Kahila, Heikki; Wehrfritz, Armin; Kaario, Ossi; Vuorinen, Ville

Large-eddy simulation of dual-fuel ignition

Large-eddy simulation of dual-fuel ignition: Diesel spray injection into a lean methane-air mixture

Heikki Kahila [a],[*], Armin Wehrfritz [b], Ossi Kaario [a], Ville Vuorinen [a]

[a] *Department of Mechanical Engineering, Aalto University School of Engineering, Puumiehenkuja 5, Espoo 02150, Finland*
[b] *School of Mechanical and Manufacturing Engineering, University of New South Wales, Sydney, NSW 2052, Australia*

ARTICLE INFO

ABSTRACT

In the present study, large-eddy simulation (LES) together with a finite-rate chemistry model is utilized for the investigation of a dual-fuel (DF) ignition process where a diesel surrogate (*n*-dodecane) spray ignites a lean methane-air mixture in engine relevant conditions. The spray setup corresponds to the Engine Combustion Network (ECN) Spray A configuration enabling an extensive validation of the present numerical models in terms of liquid and vapor penetration, mixture distribution, ignition delay time (IDT) and spatial formaldehyde concentration. The suitability of two *n*-dodecane mechanisms (54 and 96 species) to cover dual-fuel chemical kinetics is investigated by comparing the predicted homogeneous IDTs and laminar flame speeds to reference values in single-fuel methane-air mixtures. LES of an *n*-dodecane spray in DF conditions is carried out and compared against the baseline ECN Spray A results. The main results of the study are: (1) ambient methane impacts the ignition chemistry throughout the oxidation process. In particular, the activation of the low-temperature chemistry is delayed by a factor of 2.6 with both mechanisms, whereas the high-temperature chemistry is delayed by a factor of 1.6–2.4, depending on the mechanism. (2) The ignition process starts from the spray tip. (3) There exists a characteristic induction time in the order of 0.1 ms between the start of the first high-temperature reactions and the time when maximum methane consumption rate is achieved. (4) The high-temperature ignition process begins near the most reactive mixture fraction conditions. (5) The role of low-temperature reactions is of particular importance for initiation of the production of intermediate species and heat, required in methane oxidation and (6) both applied mechanisms yield qualitatively the same features (1)–(5) in the DF configuration.

1. Introduction

The dual-fuel (DF) combustion concept constitutes a promising strategy for modern gas engines to achieve simultaneously low emissions of unburned hydrocarbons (UHC) as well as nitrogen and sulfur oxides (NOx, SOx). Modern gas engines operating with e.g. natural gas are reaching the desired properties with comparable efficiency to existing diesel engines [1–3]. Importantly, natural gas consists mainly of methane (CH_4) which induces naturally lower (CO_2) emissions due to the low carbon content. Natural availability, widely developed gas distribution networks (liquefied natural gas terminals), and a low fuel price promote utilization of natural gas [1,3].

In dual-fuel engines, features of conventional spark and compression ignition engines are combined. The gaseous fuel is premixed with air and compressed similar to conventional diesel engines. However, the compressed lean fuel-air mixture does not autoignite due to the long ignition delay time (IDT) which is characteristic for low-reactivity fuels like methane. Hence, a relatively small quantity of high-reactivity fuel, e.g. liquid diesel fuel, is injected into the engine cylinder at the end of a compression stroke. The high-reactivity fuel autoignites and releases enough energy to ignite the surrounding natural gas-air mixture [1]. Such an ignition mechanism is often referred to as diesel pilot ignition and is applied in many commercially available gas engines. Typically, the pilot fuel quantity is very small yet large enough to achieve a reliable ignition timing [4,5]. In general, it has been reported that

insufficient pilot ignition may lead to combustion instabilities and results in misfiring and UHC emissions [5–8]. It is worth noting that most dual-fuel engines can operate interchangeably in both, dual-fuel and conventional diesel, modes [2].

Dual-fuel combustion research has gained more attention in recent years. However, most of this research has been focused on the performance, efficiency, emissions and combustion stability issues in either research or production engine experiments [8–22]. In literature, the dual-fuel combustion concept has often been discussed alongside e.g. homogeneous charge compression ignition (HCCI) [23] and reactivity controlled compression-ignition (RCCI) [24–26] concepts, depending on the injection timing, pilot fuel quantity and stratification levels of the charge. Only a few experimental studies include more detailed optical imaging investigations on the combustion process [22,27–34]. However, only qualitative details of the diesel-methane-air autoignition and the subsequent premixed flame initiation process have been previously reported. In particular, a limited understanding of the autoignition mechanism in dual-fuel engine configurations has been noted [8,15,18,19,34].

It has been observed in engine experiments that the ignition of diesel spray is retarded if the ambient air contains methane, compared to ignition in pure air [12–14,32,34]. Recently, Schlatter et al. [32] conducted concurrent optical Schlieren and chemiluminescence experiments of the DF pilot ignition in a rapid compression machine configuration at various methane equivalence ratios. According to the experiments, pilot ignition is a volumetric process within the pilot spray envelope and there is a linear relation between the IDT and methane equivalence ratio. Recently, Srna et al. [34] supplemented these experiments by including laser diagnostics for formaldehyde detection to better identify the early low-temperature ignition stage. Both the low- and high-temperature ignition stages of the pilot fuel were reported to be delayed with an increasing ambient methane concentration. However, the temporal separation between the first formaldehyde detection and the high-temperature ignition (OH chemiluminescence) was found almost constant and independent of methane-air equivalence ratio. Such behavior indicates that methane may have a significant role on low-temperature ignition chemistry with diesel fuels. Dronniou et al. [30] observed that the ignition seems to take place in pilot fuel rich mixtures. In addition, the retarding influence of methane on the IDT is observed to increase with decreasing ambient oxidizer temperature [35,36].

Aside from the experimental work, numerical studies on diesel pilot ignited dual-fuel combustion have been reported in the literature [12,24–26,35,37–42]. These numerical studies include simplified zero-dimensional (0d) zonal models [12,37] as well as multiple Reynolds-averaged Navier–Stokes (RANS) studies of full engine configurations [24–26,38,39]. In these RANS studies, combustion is modeled by means of finite-rate chemistry integration and typically experimental in-cylinder pressure data is used for validation. However, little emphasis has been put on grid resolution, details of the pilot spray, chemical mechanism and turbulence model contribution and validation. Schlatter et al. [35] employed a more advanced combustion model in RANS computations by considering the autoignition of an *n*-heptane pilot ignition in terms of the conditional moment closure (CMC) formulation, whereas the premixed flame propagation was tracked by the level-set method.

Three studies of DF combustion with direct numerical simulation (DNS) are reported in the literature [40,42,43]. Demosthenous et al. [42] studied the evaporation and ignition of *n*-heptane droplets in CH_4-air mixtures with the presence of decaying homogeneous isotropic turbulence. The DNS results show the validity of the most-reactive mixture fraction concept, earlier found for diesel-surrogates [44]. Methane consumption is initiated due

to heat release and intermediate species originating from the *n*-heptane oxidation process. Unburned methane was reported to exist within the ignition kernels if there was an insufficient quantity of radicals and oxygen for complete combustion of both fuels.

Wang et al. [43] conducted a DNS of an *n*-heptane/methane-air laminar mixing layer. Three time windows related to DF combustion were identified: IDT of the local mixture, time to attain peak temperature and time to achieve steady flame propagation. Bhagatwala et al. [40] carried out one- and two-dimensional DNS on ignition and flame propagation for *n*-heptane/*iso*-octane mixtures under thermochemical conditions representative for RCCI. Both deflagration and spontaneous ignition fronts were observed to co-exist in the simulations.

A challenge in numerical DF combustion modeling is the choice of a chemical mechanism which should be able to cover the chemistry of both the pilot and the primary fuel. In the context of DF combustion, Burke et al. [45] successfully developed a chemical mechanism for mixtures of dimethyl ether (DME) and methane. Other attempts to facilitate the DF chemistry were carried out by Maghbouli et al. [38] and Rahimi et al. [46] who both added the major methane reaction paths into a reduced *n*-heptane mechanism. Both mechanisms showed good performance against experimental in-cylinder pressure traces in engine simulation context. The RANS study by Schlatter et al. [35] and the DNS studies [42,43] applied reduced *n*-heptane mechanisms which include methane and reproduce qualitatively the autoignition and laminar flame speed results close to the GRI 3.0 reference mechanism [35,42].

Ghaderi Masouleh et al. [36] studied the suitability of five *n*-dodecane ($n - C_{12}H_{26}$) mechanisms (detailed and reduced) for dual-fuel combustion. Extensive validations were conducted in canonical 0d-ignition and one-dimensional (1d) laminar flame configurations for pure methane-air mixtures. Due to the lack of experimental IDT and flame speed data for *n*-dodecane/methane fuel blends, only comparisons between the mechanisms were reported. It was concluded that the molar ratio of $n - C_{12}H_{26}/CH_4$ is a key factor in the homogeneous autoignition problems and the retarding influence of methane on the IDT appears due to a change in the production of intermediate species and radicals.

As the discussion above shows, the understanding of the DF ignition process and its modeling practices in realistic engine-like conditions is limited. While dual-fuel research is lacking comprehensive and fundamental experiments, such data is available for diesel and gasoline fuels within the Engine Combustion Network (ECN) [47], which is an international research collaboration facilitating experimental and computational engine research. Within the ECN, baseline target conditions together with experimental and computational guidelines have been defined for different spray flame cases. The cases selected for the current study are thus based on the ECN Spray A conditions. In particular, an ambient gas temperature of 900 K, an ambient pressure of approximately 6MPa, a molar oxygen concentration of 15% and an injection pressure of 150MPa are chosen to correspond to the ECN Spray A baseline case. In the recent years, several experimental studies have been carried out for the Spray A case [47–54] and they have inspired multiple numerical studies with a wide range of models and chemical mechanisms [55–70].

In this study the ECN Spray A configuration is chosen as a reference case representing the single-fuel (SF) diesel ignition characteristics and to provide a well-characterized framework for a numerical dual-fuel setup. This modified dual-fuel Spray A includes methane in its ambient oxidizer composition and is hereafter referred to as "DF spray". The main emphasis in the present work is on the DF ignition process in a realistic diesel spray configuration.

The main objectives of this work are to:

1. demonstrate the influence of additional methane in the oxidizer composition on the transient stages of ignition in the DF spray case,
2. compare two chemical mechanisms (54 and 96 species) in a single-fuel and dual-fuel context,
3. investigate the ignition location and the corresponding mixture state in both single-fuel and dual-fuel configurations,
4. identify the most sensitive chemical reactions with respect to the IDT.

2. Numerical methods

2.1. Gas phase governing equations

The Eulerian gas phase is described by the compressible Navier–Stokes equations. The Favre-filtered LES formulation for the continuity, momentum, species and energy equations is the following:

$$\frac{\partial \overline{\rho}}{\partial t} + \frac{\partial \overline{\rho}\widetilde{u}_i}{\partial x_i} = \overline{S}_\rho, \tag{1}$$

$$\frac{\partial (\overline{\rho}\widetilde{u}_i)}{\partial t} + \frac{\partial (\overline{\rho}\widetilde{u}_i\widetilde{u}_j)}{\partial x_j} = \frac{\partial}{\partial x_j}\left(-\overline{p}\delta_{ij} + \overline{\rho}\widetilde{u}_i\widetilde{u}_j - \overline{\rho}\widetilde{u}_i u_j + \overline{\tau}_{ij}\right) + \overline{S}_{u,i}, \tag{2}$$

$$\frac{\partial (\overline{\rho}\widetilde{Y}_k)}{\partial t} + \frac{\partial (\overline{\rho}\widetilde{u}_i\widetilde{Y}_k)}{\partial x_i} = \frac{\partial}{\partial x_i}\left(\overline{\rho}\widetilde{u}_i\widetilde{Y}_k - \overline{\rho}\widetilde{u_i Y}_k + \overline{\rho}\widetilde{D}\frac{\partial \widetilde{Y}_k}{\partial x_i}\right) + \overline{S}_{Y_k} + \overline{\dot{\omega}}_k, \tag{3}$$

$$\frac{\partial (\overline{\rho}\widetilde{h}_t)}{\partial t} + \frac{\partial (\overline{\rho}\widetilde{u}_j\widetilde{h}_t)}{\partial x_j} = \frac{\partial \overline{p}}{\partial t} + \frac{\partial}{\partial x_j}\left(\overline{\rho}\widetilde{u}_j\widetilde{h}_s - \overline{\rho}\widetilde{u_j h}_s + \frac{\overline{\lambda}}{\overline{c}_p}\frac{\partial \widetilde{h}_s}{\partial x_j}\right) + \overline{S}_h + \overline{\dot{\omega}}_h, \tag{4}$$

where $\overline{\rho}$, $\widetilde{u}_i$, $\overline{p}$, $\widetilde{Y}_k$, $\widetilde{h}_s$, $\overline{\tau}_{ij}$, denote the filtered density, velocity, pressure, species k, sensible enthalpy and viscous stress tensor, respectively. In particular, the overbar denotes an unweighted ensemble average, whereas the tilde ($\sim$) denotes a density-weighted ensemble average. A unity Lewis number is assumed for all species, and thus $D = \lambda/(\rho c_p)$ with c_p and λ denoting the heat capacity and thermal conductivity of the gas mixture, respectively. In Eq. (4) the total enthalpy $\widetilde{h}_t$ is defined as a sum of the sensible enthalpy and the specific kinetic energy,

$$\widetilde{h}_t = \widetilde{h}_s + \frac{\widetilde{u}_i\widetilde{u}_i}{2}. \tag{5}$$

The viscous stress tensor is defined as

$$\overline{\tau}_{ij} = \overline{\mu}\left(\frac{\partial \widetilde{u}_i}{\partial x_j} + \frac{\partial \widetilde{u}_j}{\partial x_i} - \frac{2}{3}\frac{\partial \widetilde{u}_k}{\partial x_k}\delta_{ij}\right), \tag{6}$$

where $\overline{\mu}$ is the dynamic viscosity. The source terms $\overline{S}_\rho$, $\overline{S}_{u,i}$, $\overline{S}_{Y_k}$ and $\overline{S}_h$ allow the coupling between liquid and gaseous phases with respect to mass, momentum, species and energy. The reaction rate for the species k is denoted by $\overline{\dot{\omega}}_k$ and the heat release rate (HRR) in Eq. (4) is formulated as $\overline{\dot{\omega}}_h = \sum_k \Delta h_{f,k}^o \overline{\dot{\omega}}_k$, where $\Delta h_{f,k}^o$ is the enthalpy of formation. Finally, the system of equations is closed by the filtered ideal gas law.

2.2. Discretization of the governing equations

The governing Eqs. (1)–(4) are solved using the finite volume method. The time integration is based on an implicit, three time-level, and second-order accurate scheme. The diffusion terms are discretized by a 2nd-order central scheme, whereas the interpolation of the convective fluxes is treated by a non-linear flux limiter [71], similar to our previous spray studies [68,70]. The pressure-velocity coupling is implemented in terms of the reacting PISO (Pressure Implicit with Splitting of Operator) algorithm [72].

Here, the Lagrangian particle tracking method is applied to model the injected liquid phase with a model setup equivalent to our previous works on Spray A [57,70]. The primary breakup is considered by sampling computational parcels from the Rosin-Rammler size distribution with parameters that lead to an initial Sauter mean diameter of 6 μm. The secondary break-up is modeled by the KHRT model [73,74]. Heat and mass transfer between the two phases is modeled according to the standard correlations by Frössling [75] and Ranz and Marshall [76,77]. The current implementation is based on the OpenFOAM-2.4.x spray solver [78].

2.3. Subgrid-scale modeling

The unclosed LES subgrid terms in Eqs. (2)–(4) can be modeled explicitly by introducing additional dissipation via an explicit sub-grid scale model. Alternatively, such dissipation can be introduced and implicitly controlled locally by choosing a dissipative numerical scheme for the convection terms. Here, similar to the previous Spray A studies [68,70], our choice is such an implicit LES (ILES) as implemented via the non-linear flux limiter, termed as the Gamma scheme [71]. We use ILES as a "stand-alone" turbulence model without an any explicit term for a subgrid scale dissipation. The Gamma scheme requires an input parameter, k, which is chosen in order to control and maintain the spatial accuracy. In particular, we chose $k = 0.3$ for the momentum equation while $k = 1.0$ is chosen for the scalars to ensure a bounded total variation diminishing solution (a low value indicates less dissipation). The values are chosen based on our previous numerical tests in Ref. [70]. Theoretical work on the similarity between the implicit and explicit SGS models has been carried out in Refs. [79–81]. Previously, the ILES approach has been applied to free shear flows [82,83], supersonic jets [84,85], supersonic combustion [86] and non-reacting and reacting sprays [57,68,70].

2.4. Combustion modeling

Since chemical time-scales are much smaller than fluid-dynamic ones, the filtered species reaction rates $(\overline{\dot{\omega}}_k)$ and the HRR $(\overline{\dot{\omega}}_h)$ in Eqs. (3) and (4) introduce high stiffness to the system of equations. Therefore, operator-splitting is performed to separate the transport of species and energy from the chemical reactions within a CFD time step [87–89].

Change of the thermochemical composition over a CFD time step is obtained from a solution of the system of ordinary differential equations (ODE), derived from chemical kinetics [90]. Here, the stiff ODE system is solved independently in each finite volume cell by a semi-implicit Euler method (abbr. Seulex) [91]. The Seulex algorithm belongs to the class of extrapolation methods and offers an efficient and high-order (here up to 12th order) solution for stiff problems [91,92]. The relative and absolute tolerances of the Seulex algorithm are set to 1e-6 and 1e-10, respectively, which were found sufficient in our tests as well as in Ref. [92].

The chemical source terms in Eqs. (3) and (4) are then formulated as the finite difference between the initial value and the ODE solution, being only first order accurate from the operator splitting

point of view [88,93]. However, the time step used in the current LES is 80ns, which is assumed to ensure a sufficient resolution for the operator splitting throughout the unsteady ignition problem. The maximum Courant number of 0.65 is found in the immediate vicinity of the nozzle, quickly decaying to lower values farther downstream. Similar splitting techniques with relatively small time steps have been previously applied in turbulent combustion context with successful validation against the DNS [94,95] and experimental [96,97] data.

The original reaction rate evaluation of the OpenFOAM package is replaced by an optimized implementation from the open-source package *pyJac* [90]. Furthermore, an analytical formulation of the ODE system Jacobian is applied within the Seulex algorithm (provided by the *pyJac* package). The default OpenFOAM implementation of the Seulex algorithm is modified to use optimized LAPACK routines [98] for the linear algebra operations. Secondly, the computational load of the chemistry computation is dynamically distributed over all available processors using MPI. The dynamic load balancing (i.e. optimal load distribution) is based on the local time consumption of the ODE solver.

Additionally, the chemistry computation is accelerated by a simple technique: chemistry is computed only within cells into which diesel surrogate has penetrated, i.e. mixture fraction $Z > 10^{-4}$. Otherwise, the ODE solution is mapped from a reference cell (pure oxidizer) to cells without any pilot interaction. This speeds up the computation especially at early phases of the simulation when the chemical activity is spatially confined. With the described methods, a stable and accurate chemistry solution is obtained with a maximum speed-up of two orders of magnitude, compared to the default OpenFOAM-2.4.x chemistry library.

The effect of turbulence-chemistry interactions (TCI) is considered via first order closure hypothesis, i.e. reaction rate $\overline{\dot{\omega}}_k \approx \dot{\omega}_k(\widetilde{Y}_i, \widetilde{T}, \overline{p})$ and no subgrid scale model is applied for the chemical source terms in Eqs. (3) and (4). The underlying assumption is that within the high-velocity spray the turbulence levels lead to such intense mixing that the current mesh resolution together with the direct chemistry integration capture the broadened reaction zone chemistry, leading to a sufficient solution of the ignition problem. Previously, the spray autoignition problem has been reported to be less sensitive to subgrid scale modeling parameters compared to e.g. flame stabilization problem [63,99].

Recently, Pei et al. [64] applied the same first-order hypothesis in the Spray A LES context and obtained good results with a grid spacing equivalent to the present work. Furthermore, multiple LES studies with this approach have shown a rather good agreement against experiments [96,100–104]. The good performance and minor differences with respect to other closure models have been attributed to a relatively high grid resolution [96,100,103]. For example, Fulton et al. [103] report reasonable results with an average grid resolution corresponding to half of the laminar flame thickness. As discussed in the next section, the grid spacing applied in the present study corresponds to 0.6–1.6 times the relevant laminar flame thickness estimates.

As a prerequisite for successful LES, the present model configuration should be able to reproduce the experimental IDT data for the ECN Spray A, similar to our previous study using LES-FGM (flamelet generated manifold) in the same configuration [68,70]. Such consistency will be shown later on in the paper. However, it is worth noting that the present numerical approach poses also certain potential limitations regarding TCI. The major concern is to achieve a sufficient grid resolution. For example, earlier spray-LES studies with sophisticated combustion models such as transported probability density function (TPDF) and conditional moment closure (CMC) models have been only applied in spray-LES context with a lower grid resolution compared to the present work (2 - 8 × the cell size applied in this work) [66,105–107]. The first or-

Table 1
Spray simulation specifications.

	ECN Spray A	DF
Injection parameters		
Fuel	$n - C_{12}H_{26}$	$n - C_{12}H_{26}$
Nominal nozzle diameter, D	90 μm	90 μm
Fuel temperature	363 K	363 K
Injection pressure	150 MPa	150MPa
Injection duration	Continuous	Continuous
Ambient conditions		
Temperature	900 K	900 K
Density	22.8 kg/m³	22.8 kg/m³
O_2 % (molar)	15.0	15.0
CO_2% (molar)	6.230	5.955
H_2O% (molar)	3.620	3.460
N_2 % (molar)	75.150	71.835
CH_4 % (molar)	0	3.750
ϕ_{CH_4}	0	0.5

der closure hypothesis can not be generally recommended for such resolutions which is not the case in the present study.

3. Simulation configuration

The experimental reference case for the simulations in the current study corresponds to the ECN Spray A baseline conditions [47,48] given in Table 1. Liquid *n*-dodecane is injected from a 90-μm diameter nozzle hole into a constant volume combustion vessel, where the high-pressure, high-temperature ambient conditions are achieved in a pre-burn combustion event. The molar fraction of ambient oxygen corresponds to 15% after the pre-burn event. In LES, the ambient mixture composition and temperature are initiated as uniform fields while the velocity field is set to zero. The injection profile is adopted from a virtual profile generator [108], as suggested by the ECN.

The corresponding dual-fuel case applies the same configuration as the Spray A case, but methane is added to the ambient gas composition to form a mixture with an equivalence ratio of $\phi_{CH_4} = 0.5$ (w.r.t. CH_4 only). The concentrations of other species are modified such that the molar oxygen concentration remains 15% in both cases. The specific heat (c_p) of the DF mixture deviates $\sim 5\%$ from the original oxidizer. When applying Bilger's definition for mixture fraction [109,110], the stoichiometric mixture corresponds to $Z_{st}^{SF} = 0.0435$ and $Z_{st}^{DF} = 0.0234$ in SF and DF cases, respectively. For the DF case, $Z = 0$ corresponds to a methane-air mixture with $\phi_{CH_4} = 0.5$.

The computational domain has the same volume as the experimental combustion vessel at the Sandia National Laboratories [47,48]. A uniform grid-spacing of 62.5 μm is applied within the spray envelope which has been shown to yield reliable LES results for Spray A [55,57,64,68,70]. The Kolmogorov length scales are estimated to be in the order of 1–5 μm in downstream flame region [64]. The laminar non-premixed counter-flow flamelet (cf. Section 5.4) and the premixed CH_4-air flame computations in Spray A conditions yield thermal flame thickness estimates ($T_b - T_u$)/(max(dT/dx)) $\approx$ 100 and 30 μm, respectively. Measuring the full width at half maximum of the OH species profile for the non-premixed flamelet gives a thickness estimate of $\sim$ 25 μm, close to the premixed flame thickness. Such a large scale separation between turbulence, flame thickness and grid spacing makes the current simulations still prone to possible issues with the subgrid-scale modeling. Therefore, the present study concentrates on the ignition process, neglecting the premixed flame propagation in the DF case.

In the current work, we also investigate the mesh sensitivity in the DF modeling configuration. Pei et al. [64] has shown that the IDT is increasing with increasing cell size and a sufficiently
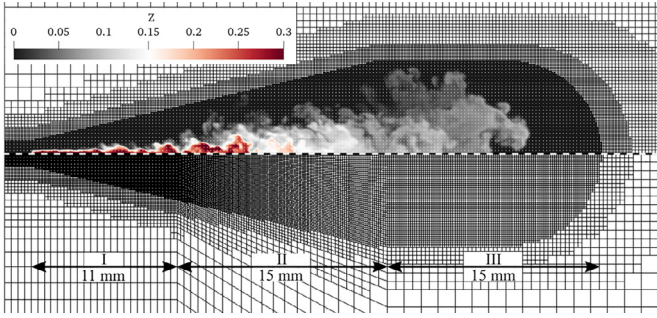
Fig. 1. Overview of a typical mixture fraction field and the applied grid resolutions: uniform 62.5 μm (top) and coarse 160 μm (bottom). The first 11 mm (I) share the uniform 62.5 μm resolution, whereas the coarse and intermediate resolution include a grading (II) from 62.5 to 80 and 160 μm, respectively.

low sensitivity of the IDT to the grid resolution is obtained with a 62.5 μm resolution. However, in their study, the chosen resolution was applied throughout the solution domain also affecting the spray development and the early mixing process. In this work, we apply a different mesh generation structure to avoid this problem and concentrate on the influence of mesh resolution on the IDT downstream where the autoignition is expected to occur.

Figure 1 presents the different grids applied in the IDT sensitivity analysis. The finest resolution has a uniform grid-spacing of 62.5 μm extending to 41mm downstream, covering the ignition locations in all cases (total cell count of 17 million). The intermediate and coarse grids are constructed in three (I-III) sections: the first 11 mm from the nozzle (I) share the resolution with the finest grid to resolve the early mixing field correspondingly to our previous studies [57,68]. Between 11 and 26 mm downstream of the injection location (II), the cell size is gradually increased to 80 (intermediate) or 160 μm (coarse). After 26 mm (III), the grids have a uniform resolution.

4. Chemical mechanism

Two chemical mechanisms are used in this work: the skeletal mechanism by Yao et al. [111] (54 species and 269 reactions) and the reduced mechanism by Frassoldati et al. [112] (96 species and 993 reactions), which are hereafter referred to as Yao and POLIMI, respectively. Both mechanisms have shown good performance in homogeneous n-dodecane-air ignition problems [111–114] and in the Spray A context: [66,111,114] (Yao) and [68,112,114] (POLIMI). However, the suitability of these mechanisms to model CH_4 chemistry has not been assessed previously.

Yao and POLIMI have 20 and 49 reactions including CH_4, respectively. In case of Yao, the share of higher hydrocarbons ($> C1$) in these reactions is 9/20 (all reversible), whereas the corresponding quantity is 28/49 (10 reversible and 18 forward) for POLIMI. The rest of the CH_4 related reactions are associated with various intermediate species such as OH, HO_2 and CH_3.

Table 2 lists 33 reactions which are considered important in the CH_4 autoignition process. The list was originally compiled by Manias et al. [115] who investigated the sensitivity of CH_4 ignition chemistry to CH_2O and H_2O_2 additives. Both additives are produced by the early low-temperature reactions in n-dodecane mixtures and thus considered to be relevant in the DF context. Table 2 shows that POLIMI covers all the reactions except (r24) and (r30), whereas Yao lacks all CH_3O_2 related reactions (r25-r31), which are relevant at low mixture temperatures $T < 1100$ K [45,115,116].

According to Table 2, both mechanisms contain the relevant subset of reactions to describe methane ignition chemistry. In order to evaluate their performance to model methane oxidation in lean conditions, we compare results from 0d constant volume

Table 2
The reactions that have an important role in the CH_4 ignition process. Superscripts 1,2,3 and 4 refer to Refs. [115], [45], [117] and [116], respectively. If a reverse reaction direction is available, it is denoted as ($\leftrightarrow$).

|	Reaction / Mechanism	POLIMI	Yao
r1[1, 2, 3, 4]	$H + O_2 \leftrightarrow O + OH$	✓	✓
r2[1]	$O + H_2 \leftrightarrow H + OH$	✓	✓
r3[1]	$OH + H_2 \leftrightarrow H + H_2O$	✓	✓
r4f[1]	$H + OH(+M) \rightarrow H_2O(+M)$	✓($\leftrightarrow$)	✓($\leftrightarrow$)
r5f[1, 2, 3, 4]	$H + O_2(+M) \rightarrow HO_2(+M)$	✓($\leftrightarrow$)	✓($\leftrightarrow$)
r6f[1, 2]	$HO_2 + OH \rightarrow H_2O + O_2$	✓($\leftrightarrow$)	✓($\leftrightarrow$)
r7f[1, 2, 3, 4]	$HO_2 + HO_2 \rightarrow H_2O_2 + O_2$	✓($\leftrightarrow$)	✓($\leftrightarrow$)
r8f[1, 2, 4]	$H_2O_2(+M) \rightarrow OH + OH(+M)$	✓($\leftrightarrow$)	✓($\leftrightarrow$)
r9f[1]	$H_2O_2 + OH \rightarrow H_2O + HO_2$	✓($\leftrightarrow$)	✓($\leftrightarrow$)
r10f[1]	$CO + OH \rightarrow CO_2 + H$	✓($\leftrightarrow$)	✓($\leftrightarrow$)
r11f[1]	$HCO + O_2 \rightarrow CO + HO_2$	✓($\leftrightarrow$)	✓($\leftrightarrow$)
r12f[1, 3]	$CH_2O + O_2 \rightarrow HCO + HO_2$	✓($\leftrightarrow$)	✓($\leftrightarrow$)
r13f[1, 2]	$CH_2O + OH \rightarrow HCO + H_2O$	✓($\leftrightarrow$)	✓($\leftrightarrow$)
r14f[1, 2]	$CH_2O + CH_3 \rightarrow HCO + CH_4$	✓($\leftrightarrow$)	✓($\leftrightarrow$)
r15f[1]	$CH_2O + HO_2 \rightarrow HCO + H_2O_2$	✓($\leftrightarrow$)	✓($\leftrightarrow$)
r16f[1, 3]	$CH_3O(+M) \rightarrow CH_2O + H(+M)$	✓($\leftrightarrow$)	✓($\leftrightarrow$)
r17f[1, 4]	$CH_3O + O_2 \rightarrow CH_2O + HO_2$	✓	✓($\leftrightarrow$)
r18f[1]	$CH_3 + H(+M) \rightarrow CH_4(+M)$	✓($\leftrightarrow$)	✓($\leftrightarrow$)
r19[1, 2, 3, 4]	$CH_4 + H \leftrightarrow CH_3 + H_2$	✓	✓
r20f[1, 2, 3]	$CH_4 + OH \rightarrow CH_3 + H_2O$	✓($\leftrightarrow$)	✓($\leftrightarrow$)
r21f[1, 2, 3]	$CH_4 + HO_2 \rightarrow CH_3 + H_2O_2$	✓($\leftrightarrow$)	✓($\leftrightarrow$)
r22f[1, 2, 3, 4]	$CH_3 + HO_2 \rightarrow CH_3O + OH$	✓($\leftrightarrow$)	✓($\leftrightarrow$)
r23[1, 2, 3, 4]	$CH_3 + HO_2 \leftrightarrow CH_4 + O_2$	✓($\leftrightarrow$)	✓($\leftrightarrow$)
r24[1, 2, 3, 4]	$CH_3 + O_2 \rightarrow CH_2O + OH$	✗	✓($\leftrightarrow$)
r25[1]	$CH_3 + O_2(+M) \leftrightarrow CH_3O_2(+M)$	✓($\leftrightarrow$)	✗
r26f[1]	$CH_3O_2 + CH_2O \rightarrow CH_3O_2H + HCO$	✓	✗
r27f[1, 2]	$CH_3O_2 + CH_4 \rightarrow CH_3 + CH_3O_2H$	✓	✗
r28f[1, 2, 3, 4]	$CH_3O_2 + CH_3 \rightarrow CH_3O + CH_3O$	✓	✗
r29f[1]	$CH_3O_2 + HO_2 \rightarrow CH_3O_2H + O_2$	✓($\leftrightarrow$)	✗
r30f[1]	$CH_3O_2 + OH \rightarrow CH_3O_2H + O_2$	✗	✗
r31f[1]	$CH_3O_2H \rightarrow CH_3O + OH$	✓($\leftrightarrow$)	✗
r32f[1, 2, 3, 4]	$CH_3 + CH_3(+M) \rightarrow C_2H_6(+M)$	✓($\leftrightarrow$)	✓($\leftrightarrow$)
r33f[1]	$C_2H_4 + OH \rightarrow C_2H3 + H_2O$	✓($\leftrightarrow$)	✓($\leftrightarrow$)
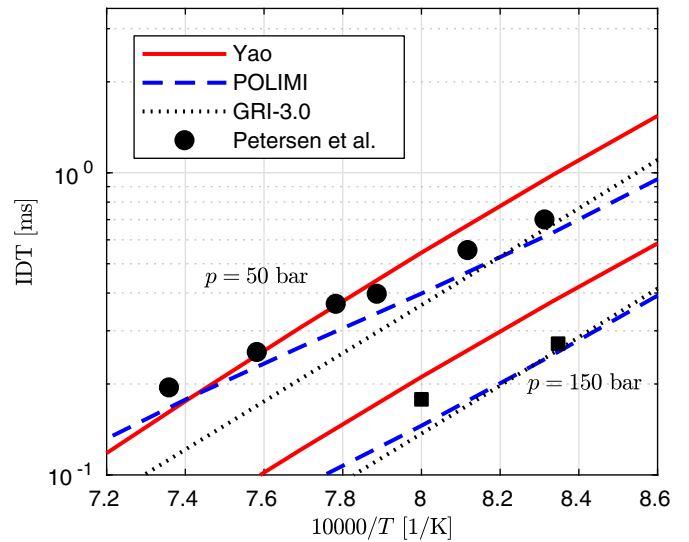
Fig. 2. IDT as a function of temperature, obtained from homogeneous reactor constant volume computations at 50 bar and 150 bar with a CH_4-air mixture corresponding to $\phi = 0.4$. Experimental data is obtained from Petersen et al. [116].

ignition computations to the experimental high-pressure (50 bar and 150 bar) shock-tube data by Petersen et al. [116]. Figure 2 shows good correlation between the experiments and 0d predictions for both Yao and POLIMI. For reference, results with the GRI-3.0 [118] mechanism are also shown. The linear slope of the temperature dependence is slightly different between the mechanisms at the 50 bar pressure and Yao predicts consistently higher IDT values compared to POLIMI and GRI-3.0 at $10000/T > 7.6$. For compar-
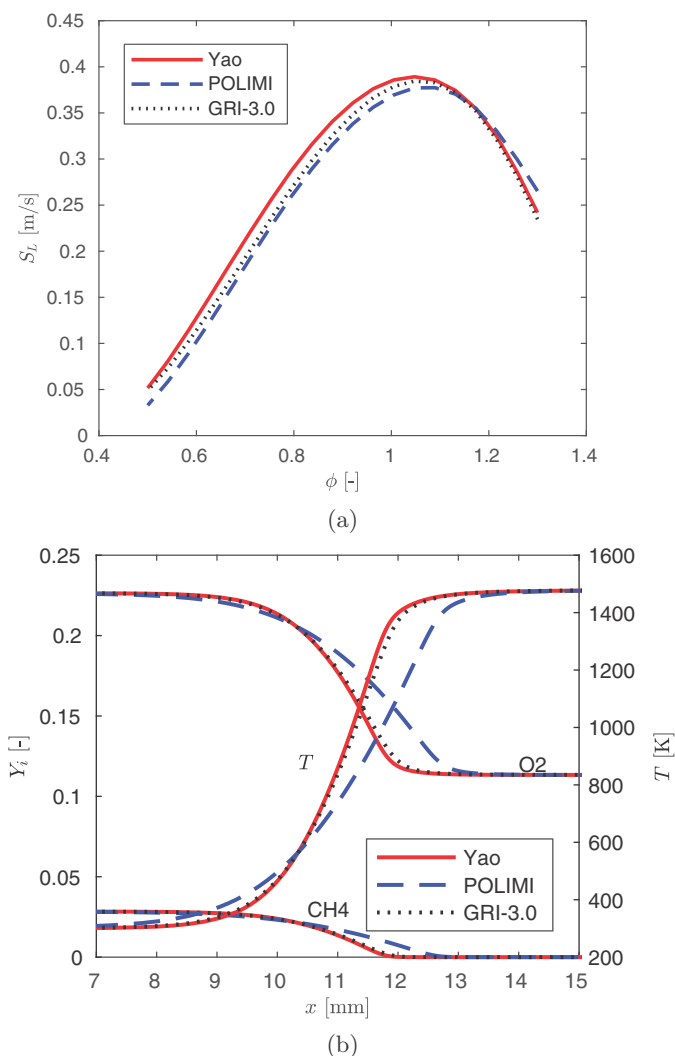
Fig. 3. One-dimensional CH_4 laminar flame speed results at 1 bar and $T_u = 300\,K$ (a) and the corresponding flame structure with $\phi = 0.5$ (b).

ison, similar analysis for *n*-dodecane-air mixtures is presented in Appendix A.

Figure 3a shows the predictions of the laminar flame speeds in methane-air mixtures at atmospheric pressure and with an unburned fuel temperature of $T_u = 300\,K$ for the Yao, POLIMI and GRI-3.0 mechanisms. The Yao and POLIMI mechanisms closely follow the GRI-3.0 mechanism over a range of equivalence ratios. In particular, Fig. 3b shows the detailed structure of the laminar flame at the prescribed conditions for all three mechanisms. Qualitatively, the profiles have a similar shape, but POLIMI predicts a slightly larger flame thickness compared to the GRI-3.0.

Overall, the selected mechanisms show good correlation between the experiments and reference solutions for the ignition and laminar flame problems in lean methane-air mixtures. In the following sections we assess the response of the selected mechanisms in a turbulent DF spray context and finally we perform a reaction sensitivity analysis with respect to the IDT in Section 5.4.

5. Results

5.1. Current understanding on diesel spray ignition

The stages of a single-fuel *n*-dodecane spray ignition process are known to consist of 1) turbulent mixing stage, 2) conse-
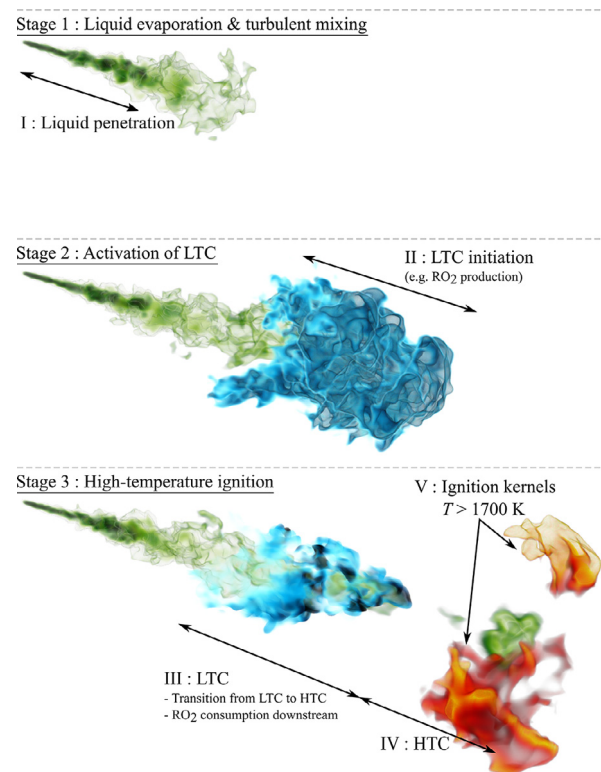

Fig. 4. Volume rendered artistic illustration of the characteristic features of a typical spray ignition process including: liquid phase and evaporation (I), early low-temperature reactions in the rich core of the spray (II), low-temperature chemistry region (III) and the high-temperature chemistry region (IV) leading to ignition kernels (V). The colors correspond to spray fuel vapor $Z > 0.08$ (green), RO_2 (blue) and $T > 1700\,K$ (orange). (For interpretation of the references to color in this figure legend, the reader is referred to the web version of this article.)

quent low-temperature reactions, and 3) high-temperature ignition [119,120]. Next, based on the present numerical results, we illustrate certain common aspects of SF and DF spray ignition. Figure 4 shows five characteristic features (I-V) of a typical turbulent spray at the time of high-temperature ignition.

The region near the nozzle (I) accounts for the high-velocity two-phase spray which is characterized by the thermophysical properties of the liquid fuel and the injection parameters, including nozzle diameter and injection pressure. The liquid penetration length is defined as the location at which most of the liquid mass has evaporated. Chemical reactions are negligible due to high flow gradients and low temperatures.

After evaporation, the injected fuel is mixing with the hot ambient gas mixture and subsequently starts to react with the available oxygen. The onset of the early low-temperature reactions is often referred to as the first-stage ignition and includes the production of various intermediate species and radicals (II), such as $C_{12}H_{25}O_2(RO_2)$, CH_2O and H_2O_2. Continuous production of such species and surrounding turbulent mixing leads to a formation of a specific low-temperature chemistry (LTC) dictated volume (III). The recent experiments by Skeen et al. [54] and multiple numerical studies [64,68–70] have shown that the prescribed process is initiated near the radial periphery of the spray before appearing across the spray as depicted in Fig. 4.

After a specific induction time, various intermediate species are starting to be consumed downstream of the LTC region (IV), and local high-temperature pockets appear around the spray tip region (V). Such pockets include species associated with high-temperature oxidation processes, such as OH, CO, and H_2O. The time instance regarding their production is referred to as the second-stage igni-

Table 3
Comparison of single-fuel (ECN Spray A) ignition delay times from LES and experiments [47,52].

	Exp.	POLIMI 62.5 μm	Yao 62.5 μm	Yao 80 μm	Yao 160 μm
IDT [ms]	0.39	0.384	0.32	0.317	0.327

tion and the spatial location is denoted as the high-temperature chemistry (HTC) region (IV).

In dual-fuel ignition systems the appearance of the high-temperature ignition kernels (V) and the surrounding LTC region are assumed to act as "chemical sparks" initiating the premixed flame propagation throughout the ambient methane-air mixture. Therefore, in this study, we are particularly interested in on the influence of ambient methane on the spatial and temporal appearance of the described regions II-V.

5.2. LES of Spray A: Ignition delay time and low-temperature chemistry ($\phi_{CH_4} = 0$)

In this section we assess the quality of the current reacting LES by investigating the sensitivity of the second-stage IDT results to the chemical mechanism and mesh resolution. For completeness, the mixture formation process in non-reacting ($Y_{O_2} = 0$) conditions is systematically validated against available experimental data in Appendix B, similar to our previous works [57,68,70]. Table 3 shows that the IDTs predicted by the present LES simulations agree fairly well with the available experimental data.

The IDTs presented in Table 3 are defined according to the ECN guidelines as the time instance τ^{2nd} at which the time derivative of the maximum temperature reaches its maximum value, i.e. $T'_{max}(t = \tau^{2nd}) = \max(dT_{max}(t)/dt)$. The current results are in line with values reported previously in literature: The mechanism by Yao et al. [111] underpredicts the IDT by $\sim 15\%$, whereas the POLIMI mechanism by Frassoldati et al. [112] predicts the experimental IDT within a 4% margin. Similar values have been reported earlier in Refs. [111,112,114,121]. We note that the present finite-rate chemistry approach yields an IDT value very close to our previous studies in which the FGM method were applied [68,70].

Table 3 also includes IDTs from LES with the Yao mechanism and three mesh resolutions: 62.5, 80 and 160 μm, (cf. Fig. 1). The three different grids yield IDT predictions within a 2% margin from one another, which is in the same scale as the Lagrangian spray-induced realization-to-realization deviations reported in Refs. [64,68]. Low sensitivity of the IDT to the grid resolution indicates that the present LES modeling approach functions consistently downstream of the end of the fine resolution region.

For further validation, Fig. 5 shows a comparison between the numerically obtained mean formaldehyde (CH_2O) field and the experimental PLIF observation by Skeen et al. [54] at $t = \tau^{2nd} - 0.1$ ms. Qualitatively, both mechanisms are able to predict the essential spatial features: the CH_2O concentration rises at ~ 12 mm and reaches its maximum after ~ 20 mm. The most distinct difference between the mechanisms is the overall length of the CH_2O rich region, being ~ 2.5 mm longer for POLIMI and can be partially explained by the longer vapor penetration at the time of ignition.

According to the presented results, the current simulation framework is considered to predict the most important features of the SF spray ignition phenomena with both chemical mechanisms. Next, the DF ignition process is investigated in the same spray configuration.
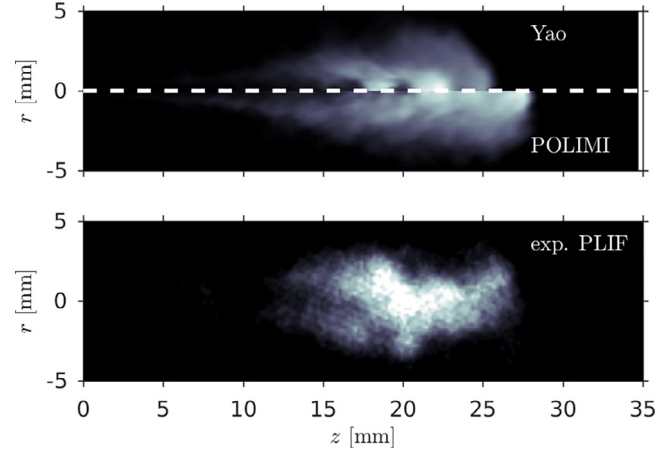

Fig. 5. Circumferential averaging of the numerical CH_2O mass fraction field (top) and the corresponding experimental PLIF sample [54] (bottom) prior to ignition at $t = \tau^{2nd} - 0.1$ ms.

5.3. LES of dual-fuel spray ($\phi_{CH4} = 0.5$)

The following sections include results on the ignition characteristics of the DF spray case with comparison to the baseline SF spray case described above.

5.3.1. Visualization of single-fuel and dual-fuel spray ignition

Figure 6 illustrates the transient stages of the ignition process (cf. Section 5.1) for both SF (on left) and DF (on right) cases and demonstrates the delaying influence of ambient methane concentration on the low-temperature and high-temperature ignition chemistry with the Yao mechanism. Here, the dodecyl peroxy radical $C_{12}H_{25}O_2(RO_2)$ is used to visualize the LTC region [122] while CO accounts for the HTC region near the main ignition.

While the early turbulent fuel-air mixing process at $t < 0.18$ ms is equivalent for both cases, the production of RO_2 is inhibited by the presence of ambient methane in the DF case (cf. Fig. 6 Ia, Ib). Whereas the production of RO_2 in the SF case appears on the sides of the fuel rich spray core at $t \approx 0.18$ ms (Ia), the productions appears later downstream for the DF case (Ib). In particular, later analysis in Fig. 7 shows that the first-stage ignition chemistry of the DF case is delayed by a factor of 2.6 compared to the SF case.

In both SF and DF cases, the first-stage ignition is followed by a strong local heat release at the spray tip (cf. IIa, IIb in Fig. 6), where the thermochemical composition and fluid dynamical conditions are favorable for ignition [54,63,123]. Clearly, ambient methane has a retarding influence on the HTC phase of the ignition which is delayed by a factor of 2.4.

After the second-stage ignition, intermediate species are consumed and combustion end-products are formed in the spray tip region. After some time, the SF case would take a typical spray diffusion flame shape with a constant flame lift-off length [52,53,63,64,68,70]. In the DF case, the interplay of various intermediate species and the high-temperature ignition kernels initiate the consumption of ambient methane, leading to a premixed flame front, modulated by the spray induced turbulence (III).
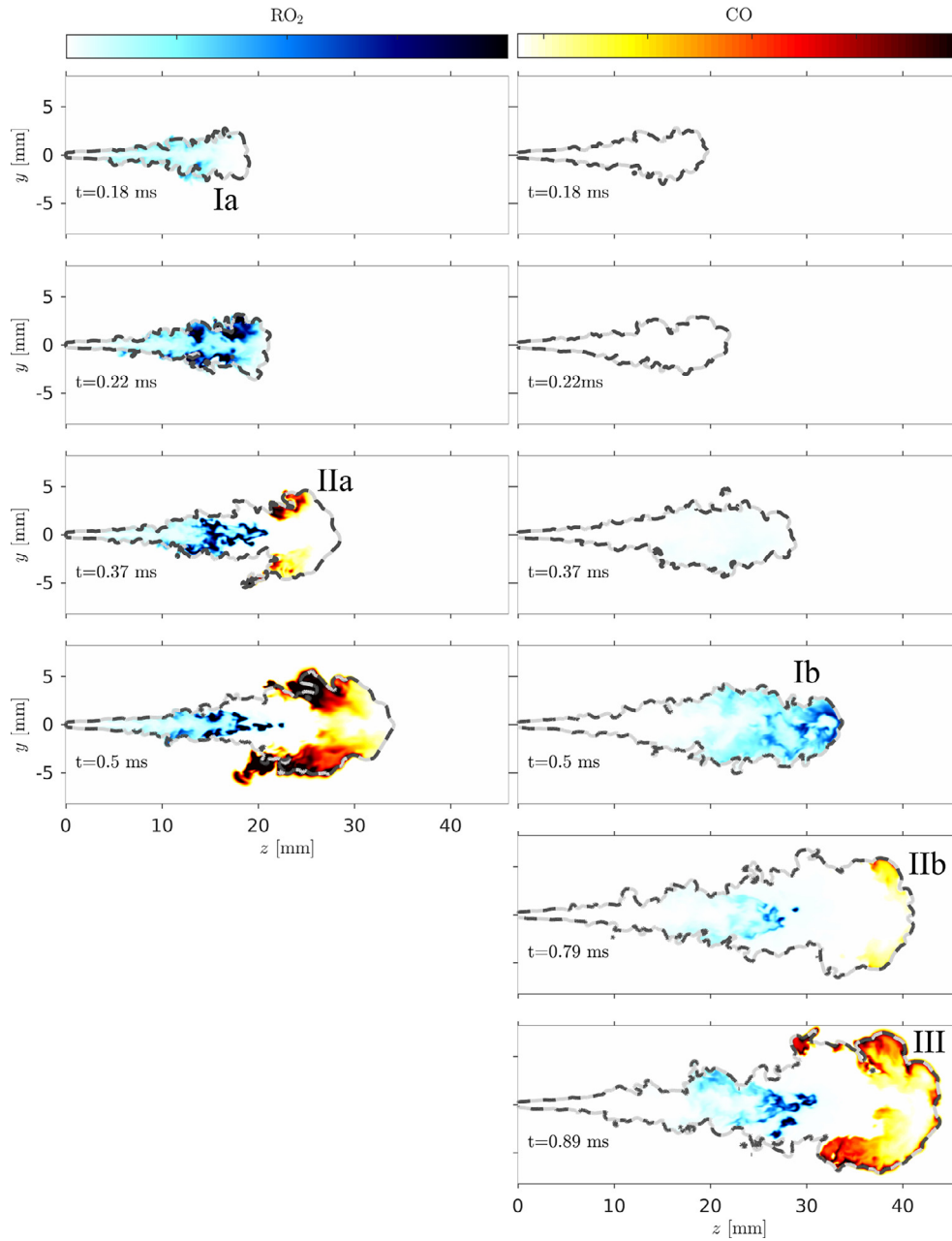
Fig. 6. Temporal evolution of RO_2 and CO fields for the SF spray (on the left) and the DF spray (on the right) with the Yao mechanism. The gray dashed contour line corresponds to stoichiometric mixture fraction.

5.3.2. Impact of ambient methane on ignition delay time

In the following, we compare the SF and DF ignition processes more in detail and confirm the qualitative result noted above: the DF spray ignition has a two-stage structure and ambient methane inhibits both, LTC and HTC. Equivalently to the SF case in Section 5.2, we report a larger sensitivity of the IDT to the chemical mechanism than to the mesh resolution.

Figure 7 shows the time evolution of maximum temperature, dodecyl peroxy radical $C_{12}H_{25}O_2(RO_2)$ and hydroxyl radical OH mass fractions for the LES cases with the Yao mechanism. The dodecyl peroxy radical is one of the first species in the decomposition path of n-dodecane and is therefore a good marker for the first-stage ignition and the LTC activity [122]. Here, we define the first-stage IDT (τ^{1st}) as the time instance when 20% of the maximum RO_2 mass fraction is reached in the system. Figure 7 shows that in the DF case the first-stage ignition is delayed by 0.29 ms com-

pared to the SF case. The present result of the inhibiting influence of methane on the LTC is consistent with the recent n-dodecane pilot injection experiments ny Srna et al. [34].

Whereas the SF spray ignites relatively quickly after the activation of the LTC, the temperature rise in the DF case takes two times longer after τ_{DF}^{1st}. The second-stage IDT (τ^{2nd}) definition is equivalent to the one applied in Section 5.2, i.e. the time instance at which dT_{max}/dt reaches its maximum in the LES domain. Furthermore, Fig. 7 shows a fast production of OH radical at $t = \tau^{2nd}$ in both SF and DF cases, indicating high-temperature ignition [119].

To elucidate the influence of the chemical mechanism on the IDT, Fig. 8 shows the first- and second-stage IDTs in SF and DF configurations for both mechanisms. The first-stage DF ignition is delayed by a ratio $\tau_{DF}^{1st}/\tau_{SF}^{1st} = 2.6$ with both mechanisms, whereas such ratios for the second-stage ignition are $\tau_{DF}^{2nd}/\tau_{SF}^{2nd} = 2.4$ and
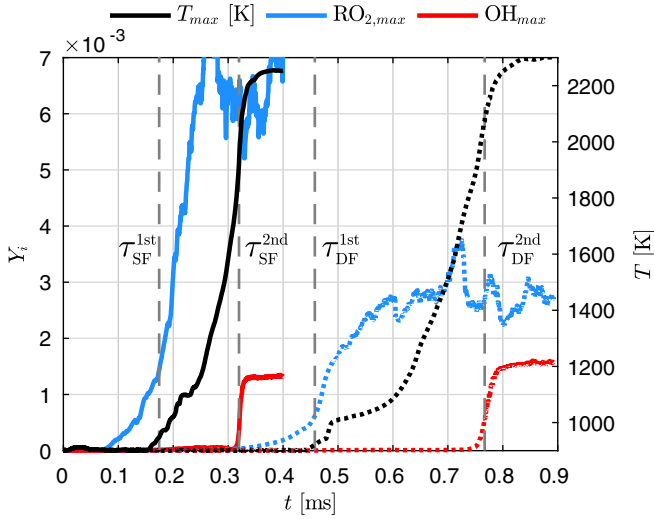
Fig. 7. Temporal evolution of the maximum $RO_{2,max}$ and OH_{max} mass fractions and temperature T_{max} for the SF (solid) and DF (dotted) cases with the Yao mechanism.
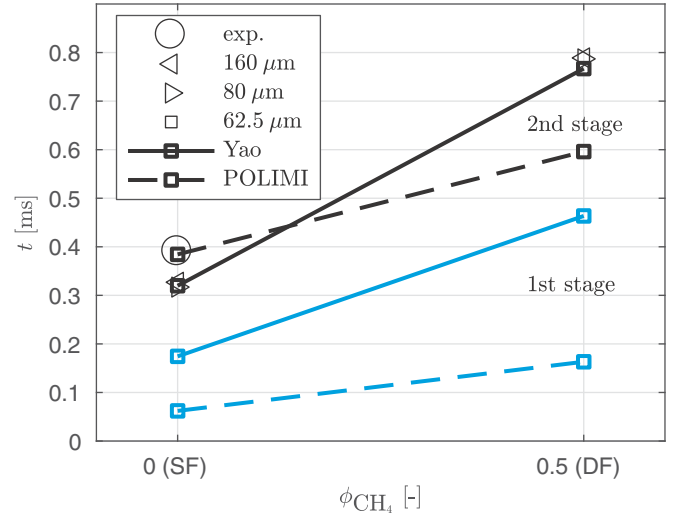

Fig. 8. First- (blue) and second-stage (black) IDTs (τ^{1st}, τ^{2nd}) for the presented SF and DF LES cases. Results with the Yao mechanism also include three different grid resolutions. (For interpretation of the references to color in this figure legend, the reader is referred to the web version of this article.)

1.6 for Yao and POLIMI, respectively. Overall, the inhibiting influence of methane on the ignition chemistry is higher for the Yao mechanism.

For completeness of the grid resolution investigation in Section 5.2, Fig. 8 shows the IDTs with the Yao mechanism for grid resolutions 62.5, 80 and 160 μm. The two cases with a coarse grid resolution are within a 4% margin from the 62.5 μm grid case. The observed 4% margin is two times larger than the deviation reported in Section 5.2 for the SF case, which is expected due to longer vapor penetration into the grid part with a coarser resolution.

5.3.3. Formation of high-temperature ignition kernels

During the n-dodecane injection process the spray region spans a broad range of mixture compositions and different spray parts

are in different thermochemical states (cf. Fig. 4). Thus, while Fig. 8 demonstrated differences in the IDTs between the SF and DF cases, it is of particular interest to explore the effect of turbulent mixing on the ignition process. Next, we visualize the DF ignition process on the cross-section plane of the spray and demonstrate similarities in LTC and HTC for the SF and DF cases in mixture fraction space. In particular, the temporal evolution of heat release and mass fractions of essential species are investigated and we show that in case of the DF spray, the ambient methane oxidation is initiated in rich mixtures.

Figure 9 shows the time evolution of the mixture fraction field for both mechanisms at time instances between τ_{DF}^{1st} and τ_{DF}^{2nd}.
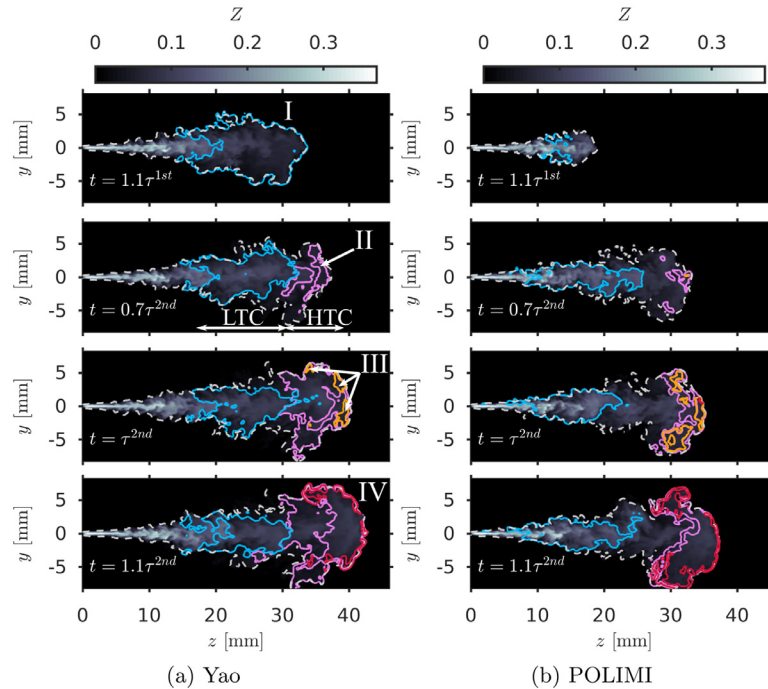

(a) Yao   (b) POLIMI

Fig. 9. DF ignition: Spatial distribution of $\widetilde{Z}$ near the time of ignition, embedded with contour lines of $1\% \max(\widetilde{Y}_{RO_2})$ mass fraction (———) and consumption rate of H_2O_2 corresponding to $1\% \min(\overline{\dot{\omega}}_{H_2O_2})$ (———). III and IV refer to contour lines of $T = 1550K$ (———) and $2\% \max(OH)$ mass fraction (———), respectively. The gray dashed line corresponds to Z_{st}.
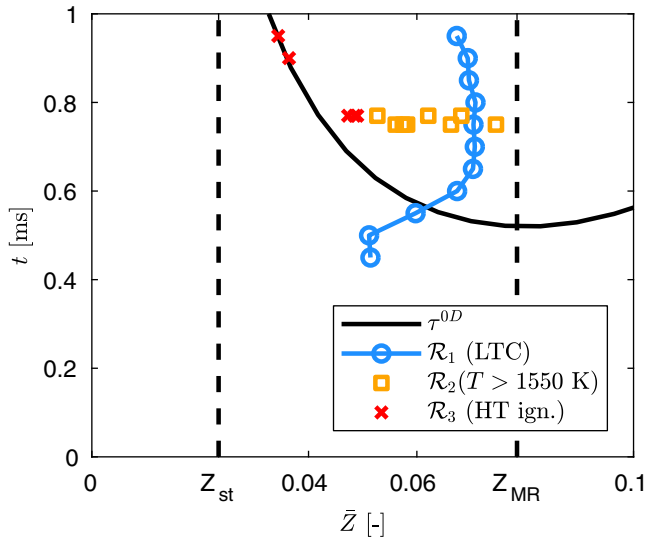
Fig. 10. Time evolution of the mean mixture fraction $\bar{Z}$ for the LTC region ($\mathcal{R}_1$) and for the appearing high-temperature (HT) ignition kernels ($\mathcal{R}_2$ and $\mathcal{R}_3$). τ^{0D} denotes the 0D simulations to compute the most reactive mixture fraction. (Results for the DF Yao case.).

The mixture fraction fields are superimposed by the blue (———) and purple (———) contour lines denoting the LTC and the early HTC regions, respectively. The LTC is defined according to the RO_2 threshold of $1\% \max(\widetilde{Y}_{RO_2})$ and the early HTC is identified with respect to the 1% threshold of the H_2O_2 consumption rate maximum (i.e. $\bar{\omega}_{H_2O_2} < 1\% \min(\bar{\omega}_{H_2O_2})$) [122].

The first row in Fig. 9 shows that the LTC extends to cover the spray tip region (I) after the first-stage ignition ($t = 1.1\tau_{DF}^{1st}$). After a certain characteristic induction time at $t = 0.7\tau_{DF}^{2nd}$, H_2O_2 starts to be consumed at the tip of the spray (II). This indicates the onset of the HTC which consumes the products of LTC.

The third row in Fig. 9 shows the formation of isolated ignition pockets (III), where the temperature exceeds 1550 K (orange contour line, ———). The interplay of various intermediate species and released heat will finally lead to the full consumption of ambient methane at the spray tip, which is visualized here by the red contour line corresponding to 2% of $\max(\widetilde{Y}_{OH})$ mass fraction (———), see region IV at $t = 1.1\tau_{DF}^{2nd}$.

Overall, the volumetric formation of ignition kernels (I-IV) is very similar to the ignition process observed in the SF spray case [64,68,70]. Figure 9 shows that the Yao mechanism predicts the appearance of the LTC region farther downstream compared to POLIMI, depicting slower LTC as also observed in Fig. 8 in terms of τ_{DF}^{1st} values. Furthermore, in case of the Yao mechanism, the H_2O_2 consumption appears relatively close to the LTC region compared to POLIMI.

In order to relate the kernel formation to the governing turbulent air-fuel mixing, Fig. 10 shows a mapping of the ignition process from physical coordinates (Fig. 9) to the mean $\widetilde{Z}t$-plane. Here, the mean mixture fraction is defined as $\bar{Z}(t) = \langle \widetilde{Z}(t, x, y, z) \,|\, \widetilde{Z} \in \mathcal{R}_i \rangle$, where $\mathcal{R}_i$ represents one of the three regions defined in Fig. 9: $\mathcal{R}_1$ represents the LTC region ($\widetilde{Y}_{RO_2} > 1\% \max(\widetilde{Y}_{RO_2})$), $\mathcal{R}_2$ corresponds to the isolated regions with $T > 1550K$ and $\mathcal{R}_3$ represents the high-temperature ignition ($\widetilde{Y}_{OH} > 2\% \max(\widetilde{Y}_{OH})$). Multiple regions belonging to either $\mathcal{R}_2$ and $\mathcal{R}_3$ were identified and selected by hand from the 3d data sets. The corresponding $\bar{Z}$ is the mean over all the data points within the individual ignition kernels.

Figure 10 shows that the formation of the LTC region begins on the rich side near $\bar{Z} \approx 2Z_{st}$ and when advancing further in time, the LTC region moves into even richer mixtures corresponding to a

spatially confined region in the jet core (cf. Fig. 9 at $t = 0.7\tau^{2nd}$). The LTC region reaches a steady state at $\bar{Z} \approx 0.07$. A continuous injection induces high momentum in richer conditions and prevents LTC at any higher mixture fractions.

The development of the high-temperature ignition kernels (denoted as $\mathcal{R}_2$) seems to begin in a broad range of rich mixtures ($2Z_{st} < \bar{Z} < 3Z_{st}$). The developing ignition kernels grow quickly and produce heat at the tip of the spray envelope. The final high-temperature oxidation is located on the outer surface of the vapor jet tip. Therefore, the corresponding mean mixture fraction values for the $\mathcal{R}_3$ region are lower but still on the rich side.

Figure 10 includes the IDT curve corresponding to the homogeneous reactor computations with initial conditions corresponding to the adiabatic mixing line. The minimum of this curve denotes the most reactive mixture fraction Z_{MR} [119]. The spray ignition process appears near the Z_{MR} values, similar to the recent results on DF ignition in homogeneous isotropic turbulence (DNS) [42].

To complete the above analysis of the ignition process, we consider next the evolution of the resolved LES statistics with respect to $\widetilde{Z}$ which 1) shows the similarities and differences between the SF and DF ignition processes and 2) indicates the $\widetilde{Z}$ values at which CH_4 oxidation is initiated. Figure 11 shows the mean profiles of T, HRR, CH_4 and CH_3 mass fractions conditioned on mixture fraction for both SF and DF cases. For brevity, only results with the Yao mechanism are shown.

For better analysis of the scattered data, we introduce conditional averages with respect to the LTC (blue) and HTC (red) regions. The LTC region is defined again as $\widetilde{Y}_{RO_2} > 1\% \max(\widetilde{Y}_{RO_2})$, whereas the HTC is defined with respect to the H_2O_2 consumption rate and temperature thresholds: $(\bar{\omega}_{H_2O_2} < 1\% \min(\bar{\omega}_{H_2O_2})) \cup (T > 1100K)$, excluding the points belonging to the LTC region.

In both SF and DF cases, the evolution of heat release rate and temperature (Fig. 11(a-b)) is similar. The early heat release appears near stoichiometry (I) and moves to more rich mixtures (II) with time. The heat release within the LTC region correlates with the formation of various intermediate species at $0 < \widetilde{Z} < 0.2$, including RO_2, CH_2O and H_2O_2. As shown by the conditional means, HTC starts on the rich side (III) but after the second-stage ignition the peak value of the mean HTC profile evolves back towards the stoichiometric conditions (IV). The peak HRR near Z_{st} corresponds to the OH radical formation at the spray tip, shown in Fig. 9.

The prescribed behavior has been earlier noted in the SF context by several authors [64,68,70,119] and the current results in Fig. 11 indicate that similar features are present in the DF case with both mechanisms. The most distinct difference between the SF and DF cases is the width of the distributions in mixture fraction space: in the SF case the mean profiles are broader and cover larger $\widetilde{Z}$ values compared to the DF case. This difference represents the inhibiting influence of methane on the chemistry in very rich mixtures in the core of the spray. Furthermore, when the ignition chemistry is delayed in the DF cases, the spray has time to penetrate farther downstream and therefore becomes more diluted, which is observed as lower $\widetilde{Z}$ values.

Even though temperature and HRR show similar features in Z-space, the influence of ambient methane becomes evident when considering the conditional mean mass fraction profiles of CH_3 and CH_4 in Fig. 11(c-d). Figure 11(c) shows that methane is produced as a part of HTC at $Z_{st} < \widetilde{Z} < 0.2$ in the SF case. Similarly, methyl radical (CH_3) is formed on the rich side as a part of the decomposition of n-dodecane [111]. However, in the DF case, there is no net production of CH_4 but its consumption begins around $\widetilde{Z} \approx 2Z_{st}$ and advances towards richer mixtures with time. After the second-stage ignition at $t = \tau^{2nd}$, the CH_4 consumption peaks in mixtures within $Z_{st} < \widetilde{Z} < 0.06$ and soon after ($t > \tau^{2nd}$) the CH_4 consumption broadens to cover $\widetilde{Z} \approx 0$ mixtures, implicating the start of flame propagation in the ambient mixture. Due to CH_4
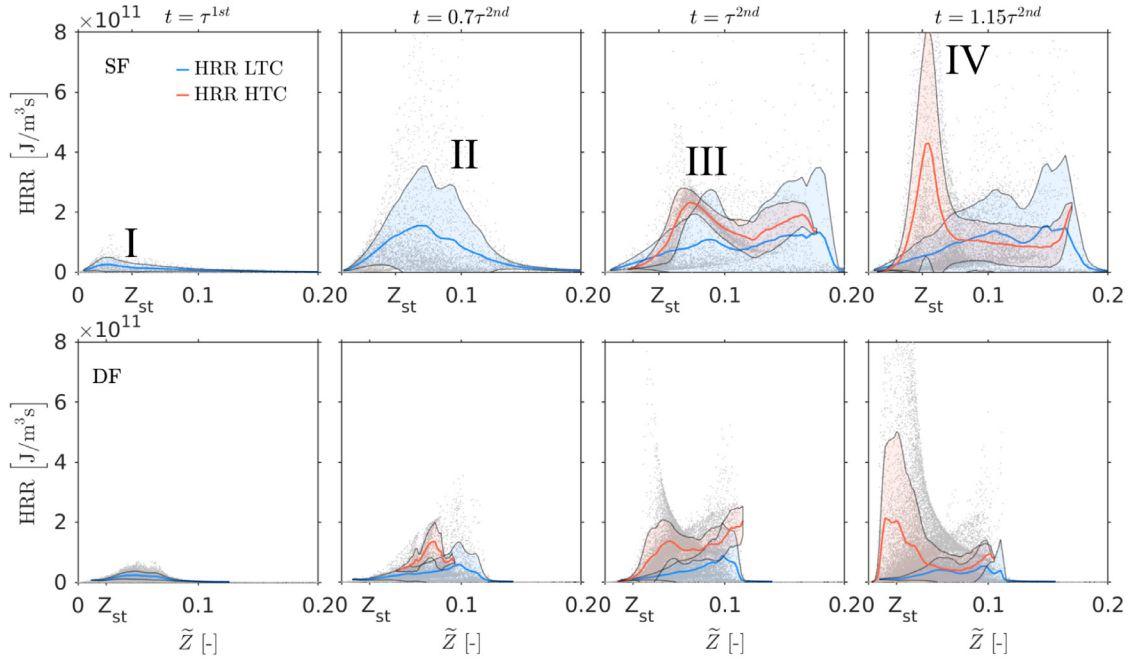
(a) HRR: SF (top) and DF (bottom).
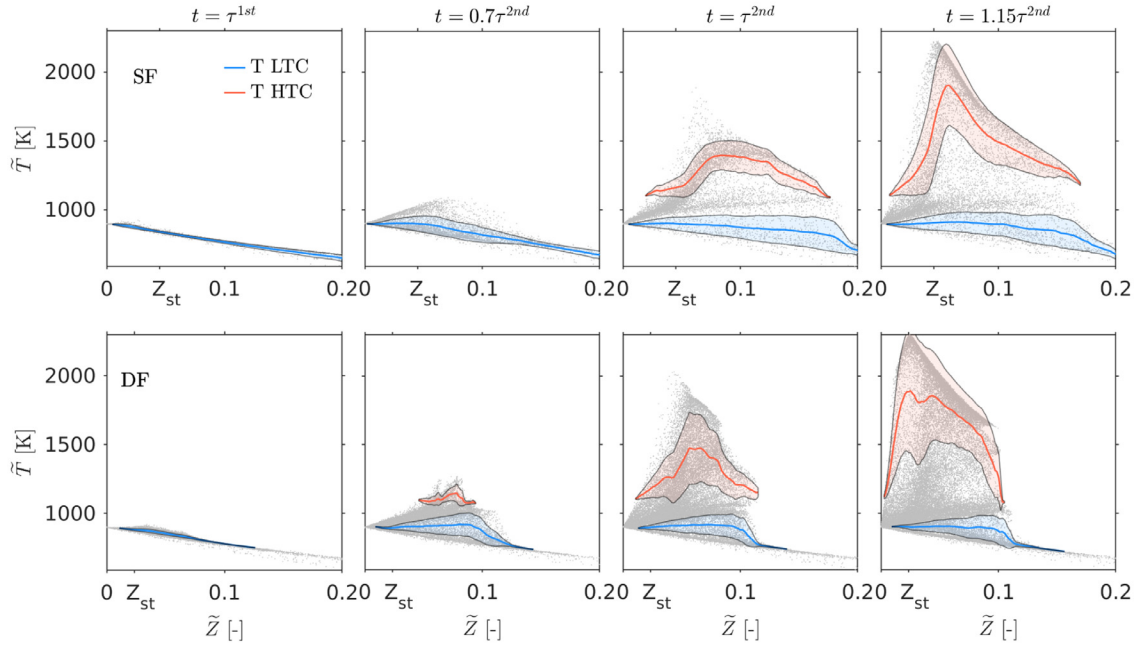
(b) Temperature: SF (top) and DF (bottom).

Fig. 11. Yao: Mean profiles (solid line) and standard deviations (filled region) of HRR (a), T (b), $\widetilde{Y}_{CH_4}$ (c) and $\widetilde{Y}_{CH_3}$ (d), conditioned with respect to $\widetilde{Z}$ and either to LTC or HTC regions, defined as $\widetilde{Y}_{RO_2} > 1\% \max(\widetilde{Y}_{RO_2})$ (LTC) and $\overline{\overline{\omega}}_{H_2O_2} < 1\% \min(\overline{\overline{\omega}}_{H_2O_2}) \cup T > 1100K$ (HTC). Only 0.5% of the data points shown in scatter (random picking).

consumption near $\widetilde{Z} = 0$, also the mean HRR appears closer to the pure oxidizer ($\widetilde{Z} = 0$) in Fig. 11(b, IV).

The distributions for the methyl radical CH_3 in Fig. 11(d) are similar for both SF and DF case prior to the second-stage ignition. However, after the second-stage ignition, the conditioning with respect to the HTC yields a clear peak in CH_3 mass fraction (V) for the SF case, whereas the CH_3 distribution appears bimodal for the DF case (VI). Such a double peak structure for the conditional mean profile appears due to the decomposition of CH_4 in both lean $Z < Z_{st}$ and rich $Z_{st} < \widetilde{Z} < 0.06$ conditions. On the lean side, species like OH, HO_2 and H can abstract the H from CH_4, producing CH_3. In

the SF case, the lack of CH_4 in the oxidizer composition prevents the methyl radical production in very lean mixtures, whereas on the rich side, CH_3 appears as a result of both CH_4 and *n*-dodecane decompositions. The consumption of CH_3 in stoichiometric conditions is due to the high-temperature oxidation at the end of the second-stage ignition, forming CO, CO_2 and H_2O.

To summarize the findings from the last two sections: The key global difference between the SF and DF sprays is the delayed ignition. We have noted that the high-temperature ignition kernel formation is a volumetric process and takes place at the tip of the spray. The time evolution and shape of statistical distributions
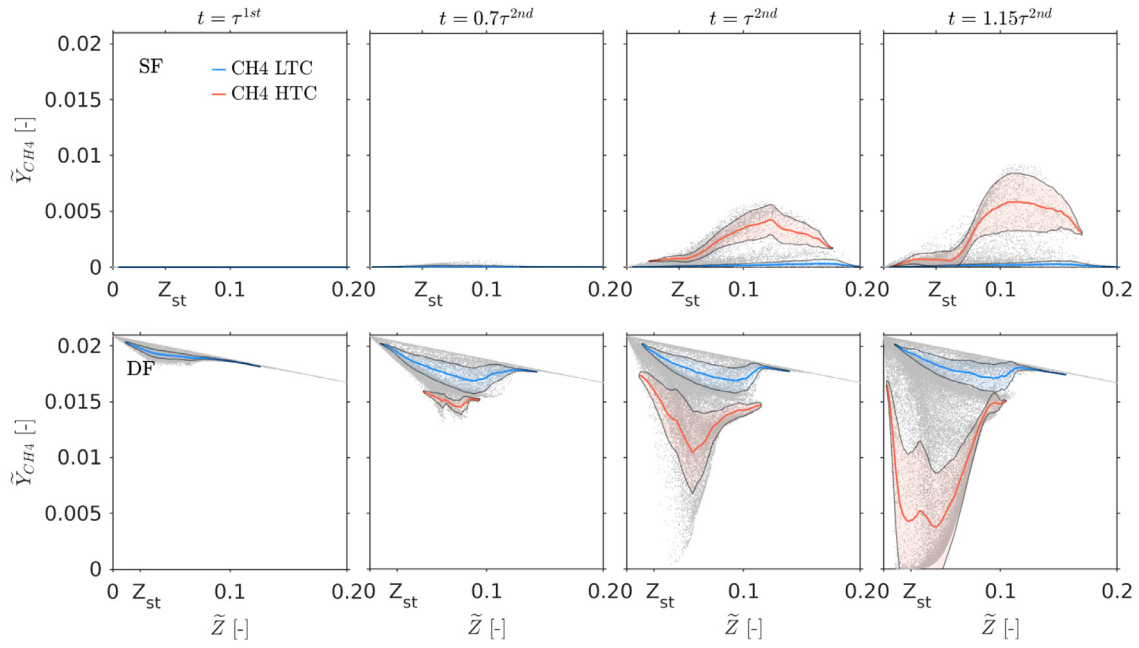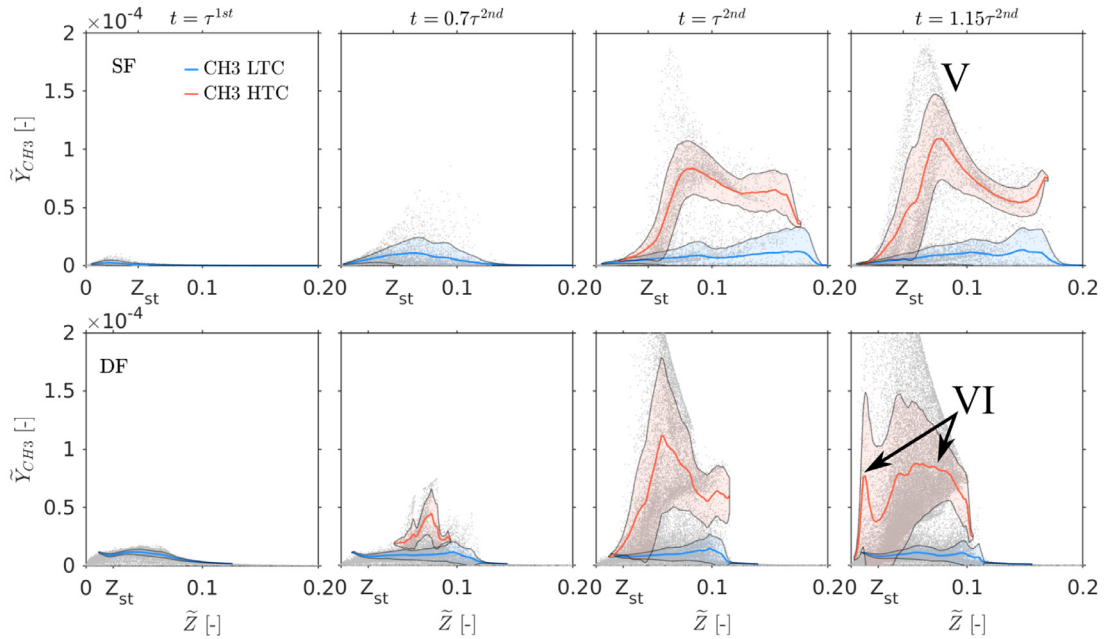
(c) CH$_4$: SF (top) and DF (bottom).

(d) CH$_3$: SF (top) and DF (bottom).

Fig. 11. Continued

in mixture fraction space are noted to be similar in both SF and DF cases: LTC begins near Z_{st} and moves to cover richer mixtures ($Z_{st} < \widetilde{Z} < 0.1$), leading to HTC near $Z \approx 2Z_{st}$. Methane is found to influence the ignition chemistry in both lean and rich conditions.

5.4. Role of methane in oxidation process of DF mixtures: 1d flames and sensitivity analysis

The LES results above clearly indicate the retarding influence of ambient methane on both first- and second-stage IDT for both chemical mechanisms. However, the means by which CH$_4$ influences the ignition chemistry seem non-trivial and have not

been discussed in previous sections. In the following sections, we demonstrate that ambient methane inhibits both LTC and HTC also in laminar configurations resembling the prescribed LES results. Furthermore, we identify the most sensitive chemical reactions in a relevant 0d ignition system and we suggest explanations for the delaying influence of ambient CH$_4$ on ignition chemistry in laminar and turbulent conditions.

5.4.1. DF ignition process in 1d flames

A widely used canonical setup to study non-premixed combustion is given by laminar counter-flow diffusion (CD) flames, in which opposing fuel and oxidizer streams form a reaction zone
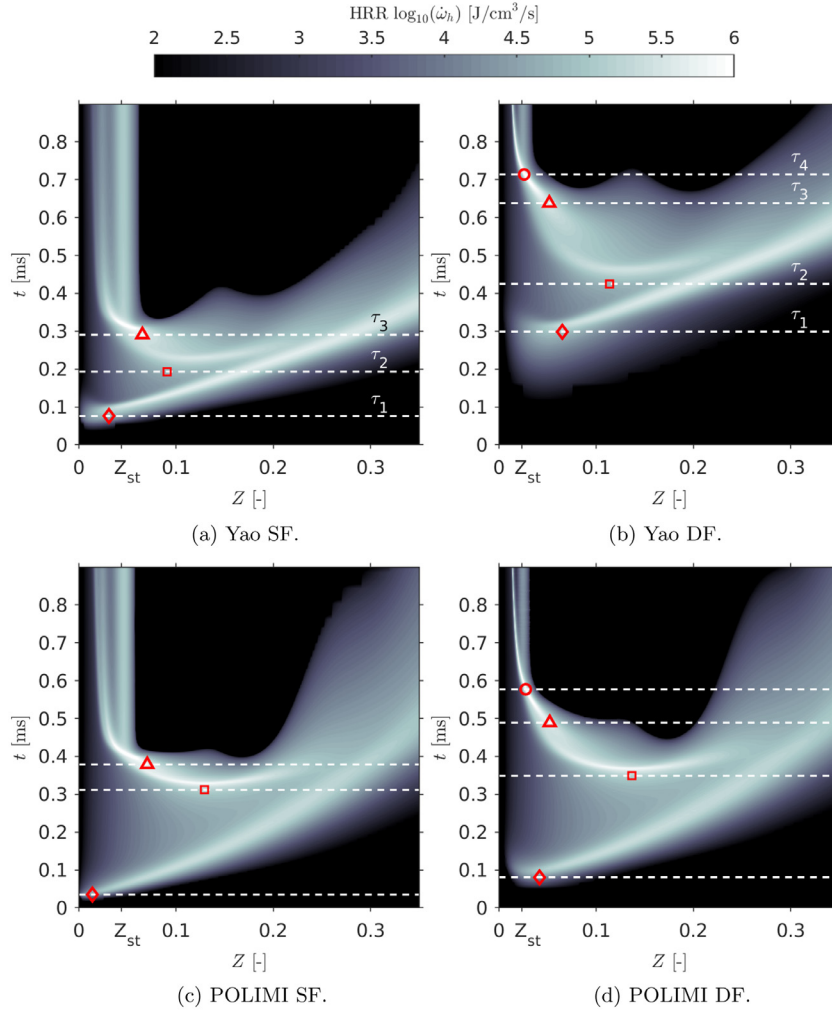
Fig. 12. Heat release rate of laminar flamelets in Zt-plane for SF (a,c) and DF (b,d) cases. Point-pairs $Z\tau$ mark the first time instance when: $\widetilde{Y}_{RO_2} > 20\% \max(\widetilde{Y}_{RO_2})$ ◊, H_2O_2 consumption rate reaches 1% of its maximum □ and OH mass fraction △ and CH_4 consumption rate ○ exceed 2% and 90% of their maximum, respectively.

close to their stagnation plane. The laminar CD flames are often applied in the analysis of complex turbulent combustion systems [69,70], motivating the application of the CD flame configuration to the DF context.

The set of governing 1d equations describing the transient igniting CD flames, i.e. flamelets, is presented in Refs. [124–126] and the solution is obtained with the Chem1D [126] software. The mixture composition and temperature at the fuel and oxidizer streams are set according to Table 1 and unity Lewis numbers are assumed for all species. Furthermore, a constant strain rate of 500 s^{-1} is applied as a model parameter, similar to our previous Spray A studies [68,70].

Figure 12 shows the HRR of the flamelet solutions in Zt-plane for both mechanisms. We have identified specific time instances $\tau_1 - \tau_4$ relevant to 1) onset of low-temperature reactions, 2) early onset of high-temperature chemistry, 3) high-temperature ignition and 4) full activation of CH_4 oxidation process.

The time instance τ_1 (◊) is defined equivalent to the first-stage IDT in the LES cases ($\widetilde{Y}_{RO_2} = 20\% \max(\widetilde{Y}_{RO_2})$), which illustrates clearly the retarding influence of methane: $\tau_1^{DF}/\tau_1^{SF} = 3.9$ for Yao and 2.3 for POLIMI. For the SF cases, the $Z\tau_1$ point is located on the lean side whereas for the DF cases it appears on the rich side.

When advancing further in time, the HRR extends towards higher mixture fraction values where the production of LTC re-

lated species is increasing. Such transition towards richer mixtures is similar for both mechanisms and has been identified earlier in the SF context by e.g. Dahms et al. [69] who referred to the phenomenon as a "cool-flame wave". It is worth noting that $\widetilde{Z}$ values exceeding 0.15 in the LES case would correlate with locations relatively far upstream where intense spray turbulence prevents chemical activity.

After a sufficient chemical induction time, the HTC is activating, which is identified here as the time instance $t = \tau_2$ (□) corresponding to a point at which the consumption rate of H_2O_2 attains 1% of its maximum (equivalent to the LES HTC definition). Figure 12 shows approximately a factor of two difference in the induction time $|\tau_2 - \tau_1|$ between the two mechanisms in both SF and DF configurations.

After the initiation of H_2O_2 consumption, it takes another characteristic induction time before the high-temperature second-stage ignition appears, which is depicted here by the time instance when OH mass fraction exceeds 2% of its maximum ($t = \tau_3$, △). Figure 12 shows the influence of methane addition on the induction time $|\tau_3 - \tau_2|$, which is approximately twice as long as the corresponding SF time scale. High-temperature ignition appears on the rich side $Z \approx 2Z_{st}$, similar to LES results in Fig. 10. We note that the applied threshold values for τ_i have been chosen rather arbitrarily. However, the conclusions of the analysis are insensitive

Table 4

The time instances τ_i indicated by dashed lines in Fig. 12 and their relative ratios. The ratio τ_1/τ_3 deviates the most between the mechanisms, indicating a different response to the low-temperature chemistry.

Mech. / t [ms]	τ_1	τ_2	τ_3	τ_4	τ_1/τ_3	τ_2/τ_3	τ_1/τ_4	τ_2/τ_4	τ_3/τ_4
Yao (SF)	0.076	0.19	0.29	–	0.26	0.66	–	–	–
POLIMI (SF)	0.035	0.31	0.38	–	0.09	0.82	–	–	–
Yao (DF)	0.30	0.43	0.64	0.71	0.47	0.67	0.42	0.60	0.89
POLIMI (DF)	0.081	0.35	0.49	0.58	0.17	0.71	0.14	0.60	0.85

to the chosen threshold values. Further information is provided in Appendix C.

In the DF case, the appearance of a typical high-temperature ignition marker (e.g. OH) does not necessarily indicate the point at which the premixed CH_4 flame is initiating. Therefore, we also show in Fig. 12 the point at which CH_4 consumption rate exceeds 90% of its maximum (τ_4, O). Such consumption rates occur for both mechanisms near the stoichiometric mixture, approximately 0.1ms after $t = \tau_3$. Minor CH_4 consumption ($\sim 5\%$ of the maximum) is observed already at earlier times ($t > \tau_1$) due to reactions with various intermediate species. The influence of CH_4 on the early ignition chemistry is further discussed in the following Section 5.4.2. A detailed description of the time evolution of H_2O_2 and CH_4 net reaction rates in Zt-plane can be found from Appendix C as well. The presented flamelet results indicate that the IDT definition should be carefully considered in DF ignition problems. In brief, the DF IDT definition should not only correlate with CH_4 consumption but also with the relevant HTC, such as high OH production. We note that the DF IDT cannot be consistently defined according to a constant maximum temperature threshold. For example, a threshold of 1250K would correspond to a time instance $t = \tau_2$ in the presented flamelet analysis and would not estimate a sufficient time scale for the premixed flame initiation (high CH_4 consumption).

Table 4 shows the time instances τ_i normalized with the high-temperature ignition delay times $\tau_{3/4}$. The largest relative difference between the mechanisms is noted with respect to ratio τ_1/τ_3, whereas the other relative ratios are rather similar. Such deviations highlight the sensitivity of ignition problems to low-temperature chemistry, which is also noted from the LES results and further discussed in Section 5.4.2.

The presented 1d flamelet results support the findings from the spray LES cases and can be summarized as follows: 1) CH_4 impacts the chemistry throughout the ignition process but the key global difference is the IDT. 2) CH_4 delays the onset of the LTC, 3) CH_4 delays the onset and final stages of the HTC, i.e. both H_2O_2 consumption and OH production phases are delayed. 4) The relative activation time of the first-stage ignition chemistry (τ_1/τ_3) is noted to deviate the most between the two mechanisms. However, despite the absolute differences in IDT values, the important qualitative features of methane influence are captured similarly by both mechanisms.

5.4.2. Reaction sensitivity analysis of DF mixtures

As a numerical experiment, we modified the Yao and POLIMI mechanisms by adding a new imaginary species CH_4^{IM} which shared the thermodynamic properties of methane but was otherwise considered as an inert gas. The laminar CD flamelet simulations were repeated in the DF configuration with CH_4^{IM} replacing CH_4 in the oxidizer mixture. The resulting change in mixture thermodynamic properties, such as c_p, accounted only for $\sim 1\%$ change in the flamelet IDT. Such a negligible difference suggests that CH_4 must influence the ignition chemistry via reaction kinetics.

Therefore, brute-force sensitivity analyses are executed to determine the reactions that have the greatest influence on the second-stage IDT. The following analysis evidently shows that the additional CH_4 influences the chemical pathways and production/consumption rates of intermediate species such as OH, CH_3, HO_2 and early decomposition products of n-dodecane such as RO_2.

The sensitivity analysis incorporates 0d homogeneous reactor computations in three initial mixture compositions corresponding to the overall equivalence ratio of $\phi = 0.5$, $\phi = 1.0$ and the most reactive mixture fraction Z_{MR}, sampled from the mixing line. The sensitivity coefficients S_i are defined as a relative change in the corresponding second-stage IDT (τ^{2nd}) when multiplying the rate constant k_i by a factor of two [111,127]:

$$S_i = \frac{\partial \tau^{2nd}}{\partial k_i} = \frac{\tau^{2nd}(2k_i) - \tau^{2nd}(k_i)}{\tau^{2nd}(k_i)}. \tag{7}$$

Negative sensitivity coefficients denote a promoting influence (i.e. decreasing IDT), whereas the positive coefficients denote an inhibiting effect (i.e. increasing IDT).

Figure 13 shows the sensitivity analysis for the Yao (a-b) and POLIMI (c-d) mechanisms with SF and DF mixtures, respectively. Figure 13(a) and (c) depict that in the SF cases τ_{SF}^{2nd} is sensitive to the reactions related to the early n-dodecane decomposition (reactions with C_{12}-hydrocarbons). In addition, HTC related inhibiting reactions such as the chain terminating reaction $HO_2 + OH \Leftrightarrow H_2O + O_2$ (r11), have an impact on ignition characteristics in both mechanisms.

Figure 13(b) and (d) show the sensitivity analysis results for the corresponding DF cases. Common for both mechanisms is the appearance of the inhibiting reaction $CH_4 + OH \Rightarrow CH_3 + CH_2O$ (r20f) which produces methyl radicals and water from methane via H abstraction. The influence of the r20f reaction on the other reactions can be identified from Fig. 13(b): Firstly, the increased methyl radical production yields higher CH_3 mass fractions which leads to the subsequent recombination reaction $2CH_3(+M) \Rightarrow C_2H_6(+M)$ (r32f) forming ethane and to the chain terminating reaction $CH_3 + HO_2 \Rightarrow CH_4 + O_2$ (r23f) which are both known to be strongly inhibiting [115,122]. Secondly, the reactions r20f and r23f consume OH and HO_2 radicals, subsequently preventing LTC reactions where they are present as reactants (e.g. the H abstraction: $NC_{12}H_{26} + OH \Rightarrow H_2O + NC_{12}H_{25}$). This partially explains the lower HRR at $\widetilde{Z} > 0.1$ in LES statistics (cf. Fig. 11(a)). The impact of methane on the methyl radical formation in the LES case is well depicted by conditional statistics in Fig. 11(d).

What is notable in the current analysis is that the most sensitive reactions in the DF cases involve mostly the same reactions as the SF case. The DF ignition chemistry seems to be dictated by reactions involving n-dodecane and its long hydrocarbon radical products. In particular, for the POLIMI mechanism, the strongest influence of CH_4 is limited to r20f. Reactions such as r32f and r23f are present but their influence is shadowed by reactions involved with the early n-dodecane decomposition. Such dictation of n-dodecane can be considered to partially explain the smaller
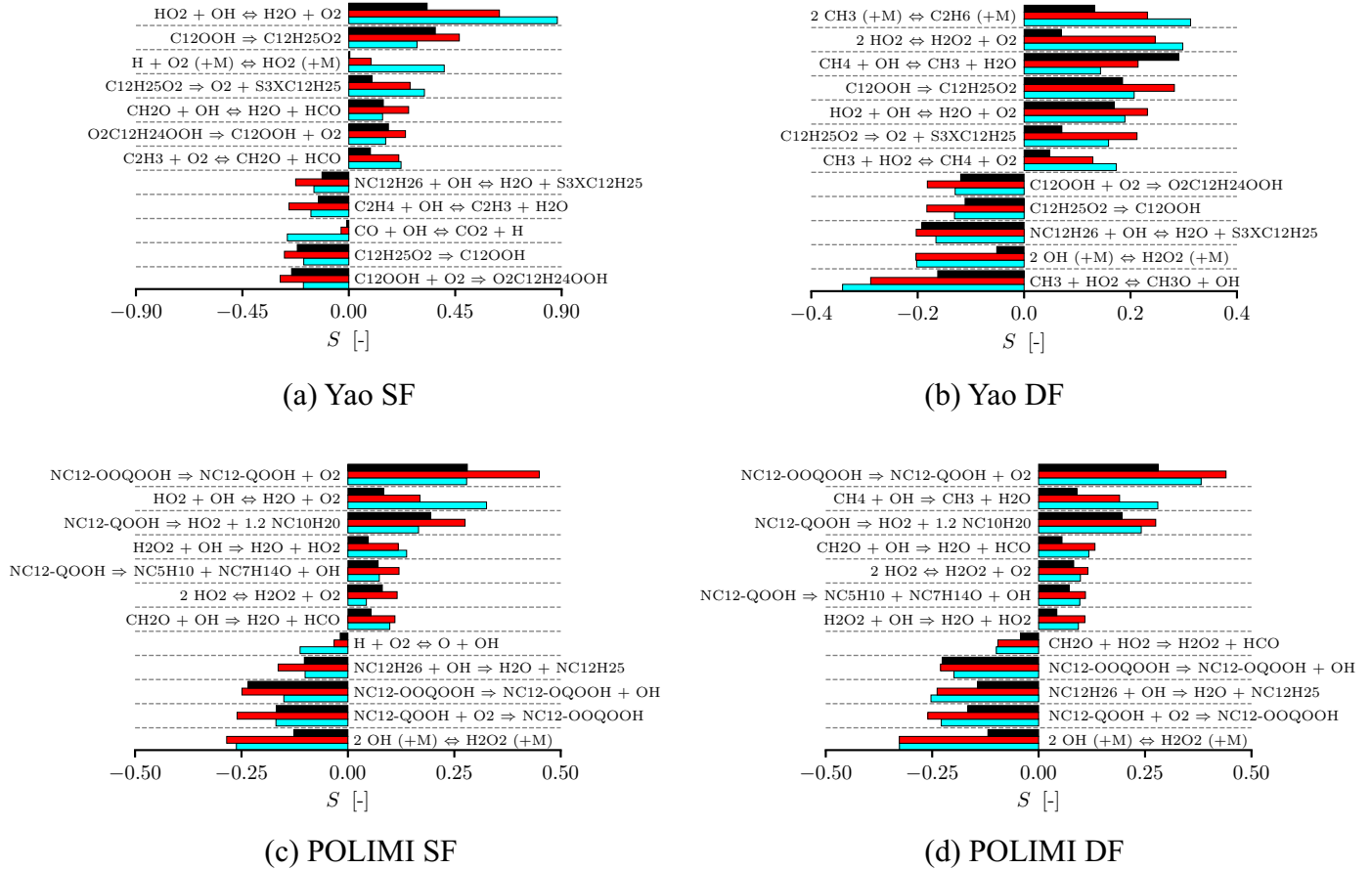
(a) Yao SF

(b) Yao DF

(c) POLIMI SF

(d) POLIMI DF

Fig. 13. Sensitivity analyses with respect to the second-stage IDT in three mixture compositions corresponding to $Z_{\phi=0.5}$ (■), Z_{st} (■) and Z_{MR} (■).

$\tau_{\text{DF}}^{\text{2nd}}/\tau_{\text{SF}}^{\text{2nd}}$ ratio observed in the LES case with the POLIMI mechanism.

The presented sensitivity analysis is in line with the work by Burke et al. [45] who showed that the most sensitive reactions in the homogeneous DME-CH$_4$-air ignition process (0d) involve DME and its immediate product species. Current results indicate that including only CH$_4$ relevant reaction pathways (cf. Table 2) to the chemical mechanism should not be considered sufficient, but the influence of methane on the early decomposition of long hydrocarbons should be considered in detail when working with DF applications.

6. Conclusions

In the present work the ignition of an *n*-dodecane spray in a lean methane-air mixture was investigated by utilizing a newly developed LES solver with finite-rate chemistry. The chemistry solution algorithm employs an analytical Jacobian and reaction rate functions adopted from the open-source chemistry package *pyJac*.

The simulations are based on the Engine Combustion Network Spray A case, enabling an extensive validation of the numerical framework against available experimental data on the spray mixing process, ignition delay times and optical imaging of formaldehyde within the reacting spray.

The baseline Spray A target conditions were modified to create a dual-fuel relevant model problem by adding methane to the ambient oxidizer composition with a methane-air equivalence ratio of 0.5. The rest of the original Spray A case configuration remained unaltered. The main findings of the current work on dual-fuel spray ignition are:

1. DF ignition is a volumetric process and can be separated into three stages: 1) first-stage ignition, i.e. early heat release due to low-temperature chemistry, 2) second-stage ignition at the spray tip, i.e. activation of high-temperature chemistry and 3) full oxidation of available CH$_4$ and premixed flame initiation.
2. Ambient methane influences the low- and high-temperature chemistry throughout the ignition process. Both first- and second-stage ignition processes are inhibited compared to the single-fuel reference case.
3. Chemical decomposition of *n*-dodecane produces heat, intermediate species and radicals, enabling a faster ignition compared to homogeneous ignition of pure methane-air mixtures.
4. High-temperature ignition in LES appears in rich mixtures ($Z \approx 2Z_{st}$).
5. The chemical mechanisms by Yao et al. [111] and Frassoldati et al. [112] depict the same qualitative DF ignition process with most deviation in time scales related to the low-temperature chemistry.
6. Laminar 1d igniting counter-flow flamelet computations resemble the LES results, indicating their applicability to understand the DF ignition process.
7. Sensitivity analysis shows that the ambient methane influences the early decomposition of *n*-dodecane mainly by consuming OH radical and forming methyl radicals which activate other inhibiting reactions.

Acknowledgments

Appendix A. Homogeneous ignition of *n*-dodecane mixtures

Figure A.1 shows *n*-dodecane IDT results at ambient pressures of 20bar and 40bar, with an equivalence ratio of 1.0. Constant volume assumption is applied as recommended in the corresponding experimental Refs. [128,129]. The mechanisms predict the IDT
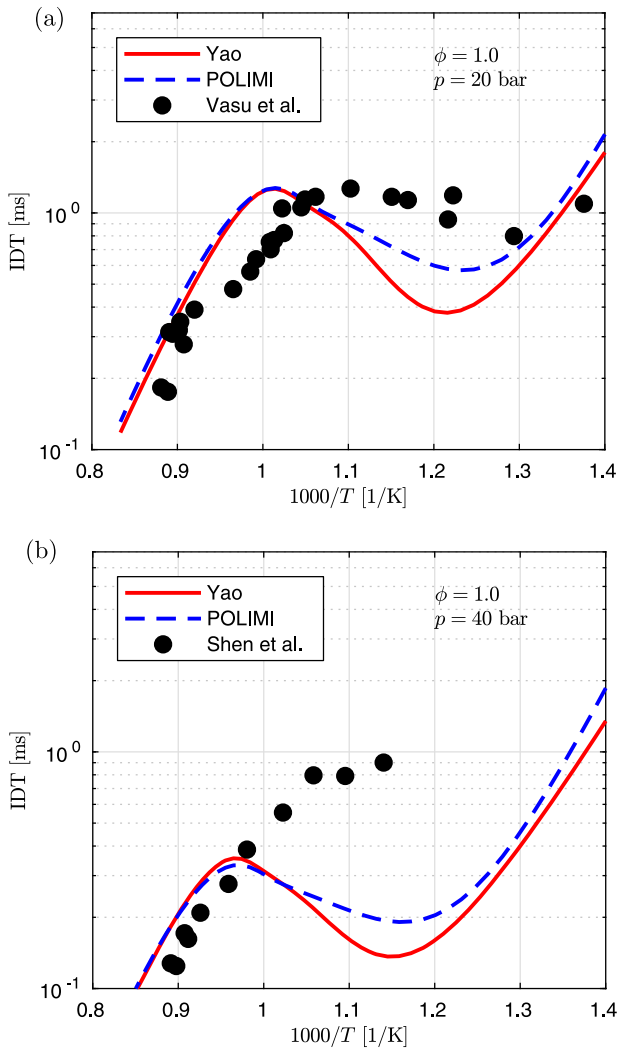
rather well at 20bar ambient pressure and high temperatures. However, increasing pressure and decreasing temperature leads to shorter IDTs compared to the shock-tube data. Results in lean conditions ($\phi = 0.5$) follow the same trend as in stoichiometric conditions (not shown). The current results are in line with the reported mechanism behavior in literature [111–114]. Interestingly, both Yao and POLIMI mechanisms have demonstrated good ignition prediction capabilities in the ECN Spray A configuration [114] and against recent experimental data from rapid compression machine measurements [113].

Appendix B. Non-reacting Spray A validation

For the non-reacting Spray A case ($\widetilde{Y}_{O_2} = 0$), experimental data for liquid and vapor penetration lengths and spatial fuel mass fraction distributions are available. A systematic validation of the current spray solver configuration in non-reacting conditions has been carried out in our previous works [57,68,70]. However, for completeness we show briefly the validation results against the available experimental data. Overall, the present LES configuration provides a fairly good agreement with the available mixing experiments [47,130].

Figure B.1 shows the liquid and vapor penetrations with comparison to the experimental data. The liquid and vapor penetrations, as specified by the ECN, are defined as the farthest axial distance with 0.1% liquid volume and gaseous fuel mass fraction. The computed vapor penetration profiles are well within the experimental error margin. The liquid penetration curve also follows closely the experimental data [47,130].

Figure B.2 shows the mean radial mixture fraction profiles at two axial locations. The profiles are obtained from a single LES realization by azimuthal and time averaging the data. The azimuthal averaging is carried out around the spray axis by dividing the domain into $N_\phi = 90$ planes. The plane data is furthermore averaged between 1.5 and 2 ms in time. The mean mixture fraction profiles are underpredicted downstream near the spray axis, whereas better agreement with experimental data is obtained after 2 mm in radial direction.
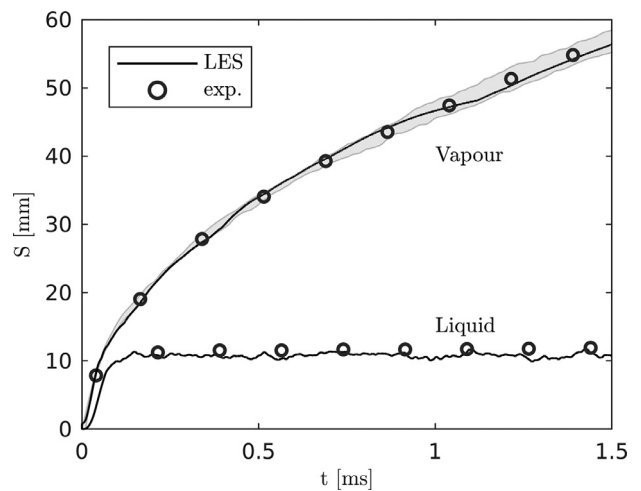

Fig. A.1. Single-fuel *n*-dodecane IDT in constant volume and with *n*-dodecane equivalence ratio of $\phi = 1.0$ at (a) 20 bar and (b) 40 bar. Experimental data is obtained from Vasu et al. [128] and Shen et al. [129].

Fig. B.1. Liquid and vapor penetration for simulated (solid lines) and experimental [47,130] (symbols) cases. The filled area is the corresponding experimental standard deviation.
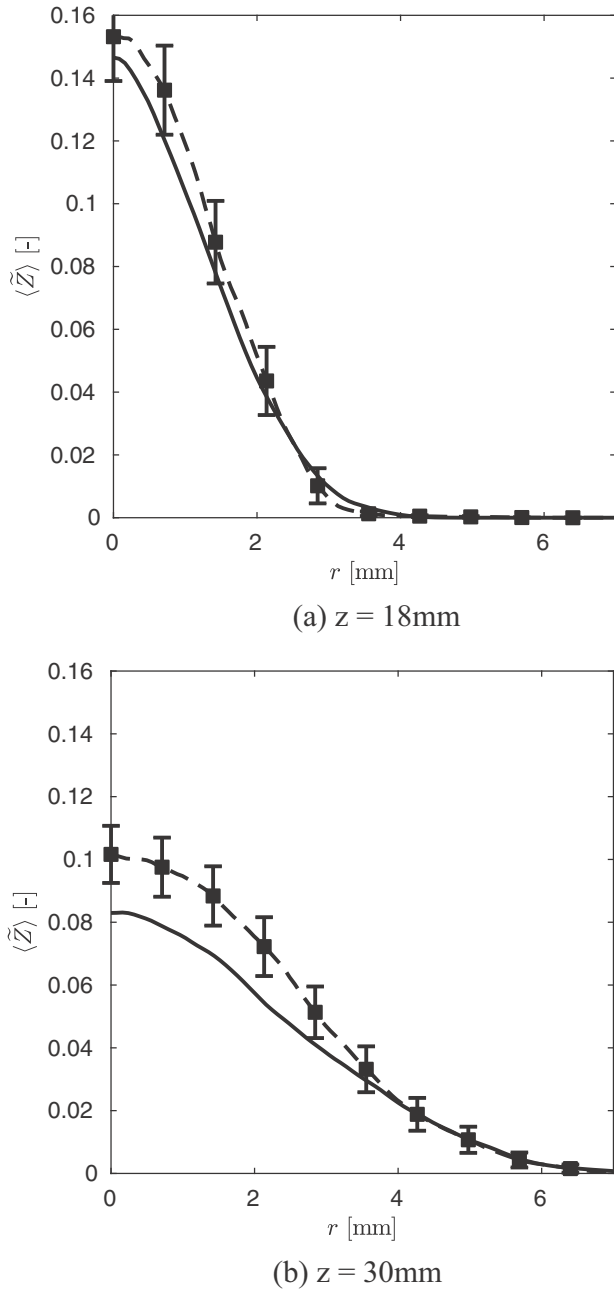
(a) z = 18mm

(b) z = 30mm

Fig. B.2. Mean mixture fraction radial profiles and experimental 95% confidence interval (error bars) at axial locations of (a) 18 mm and (b) 30 mm. Experimental data is obtained from Rayleigh-scattering imaging [47,130].

Appendix C. Time evolution of individual species in 1d flames

In Section 5.4.1 (cf. Fig. 12) four (three) timescales $\tau_1 - \tau_4$ were introduced in DF (SF) context in order to identify different ignition stages. The purpose of this appendix is to show how RO_2, H_2O_2, OH and CH_4 formation are related to the chosen timescales in laminar flames.

Figure C.1 shows the time evolution of RO_2 and OH mass fractions as well as the net reaction rates for H_2O_2 and CH_4 species for the Yao mechanism. The POLIMI mechanism was observed to yield the same features shown in Fig. C.1 (data not shown for brevity). Additionally, the time instances τ_{1-4} are shown in Zt-plane by red symbols.

Next, we discuss aspects common for SF and DF ignition. The HRR evolution in Fig. 12 can be directly related to the time evolution of species shown in Fig. C.1. As expected, the onset of early heat release (τ_1, ◇) can be associated with the early n-dodecane decomposition and following growth in RO_2 production (cf. Fig. C.1(a,b)). First low-temperature reaction paths are followed by production of other intermediate species such as H_2O_2 at rich Z values (cf. Fig. C.1(c,d)). After a sufficient time, some of these intermediate species, including H_2O_2, start to be consumed and result in locally high HRR values at $t > \tau_2$ (1% of max. H_2O_2 consumption rate, □). Finally, the high-temperature ignition takes place at $t = \tau_3$ (▲) and is denoted by a rapidly increased OH concentration (cf. Fig. C.1(e,f)).

In the DF case, n-dodecane oxidization is modified by the presence of methane, which is evident when comparing the CH_4 consumption rates between SF and DF in Fig. C.1(g,h). As discussed in Section 5.4.2, CH_4 is mildly consumed already at early times ($t \approx \tau_1$), hence influencing the n-dodecane decomposition. However, the highest consumption rates are reached after $t = \tau_3$. The process leads to a premixed flame initiation, here denoted by the threshold of 90% of the maximum consumption at $t = \tau_4$ (○).

The applied threshold values for defining τ_{1-4} are chosen rather arbitrarily but as Fig. C.1 shows, they are justified from the autoignition chemistry point of view and the characteristic ratios reported in Table 4 have been noted to be rather insensitive to the threshold values.
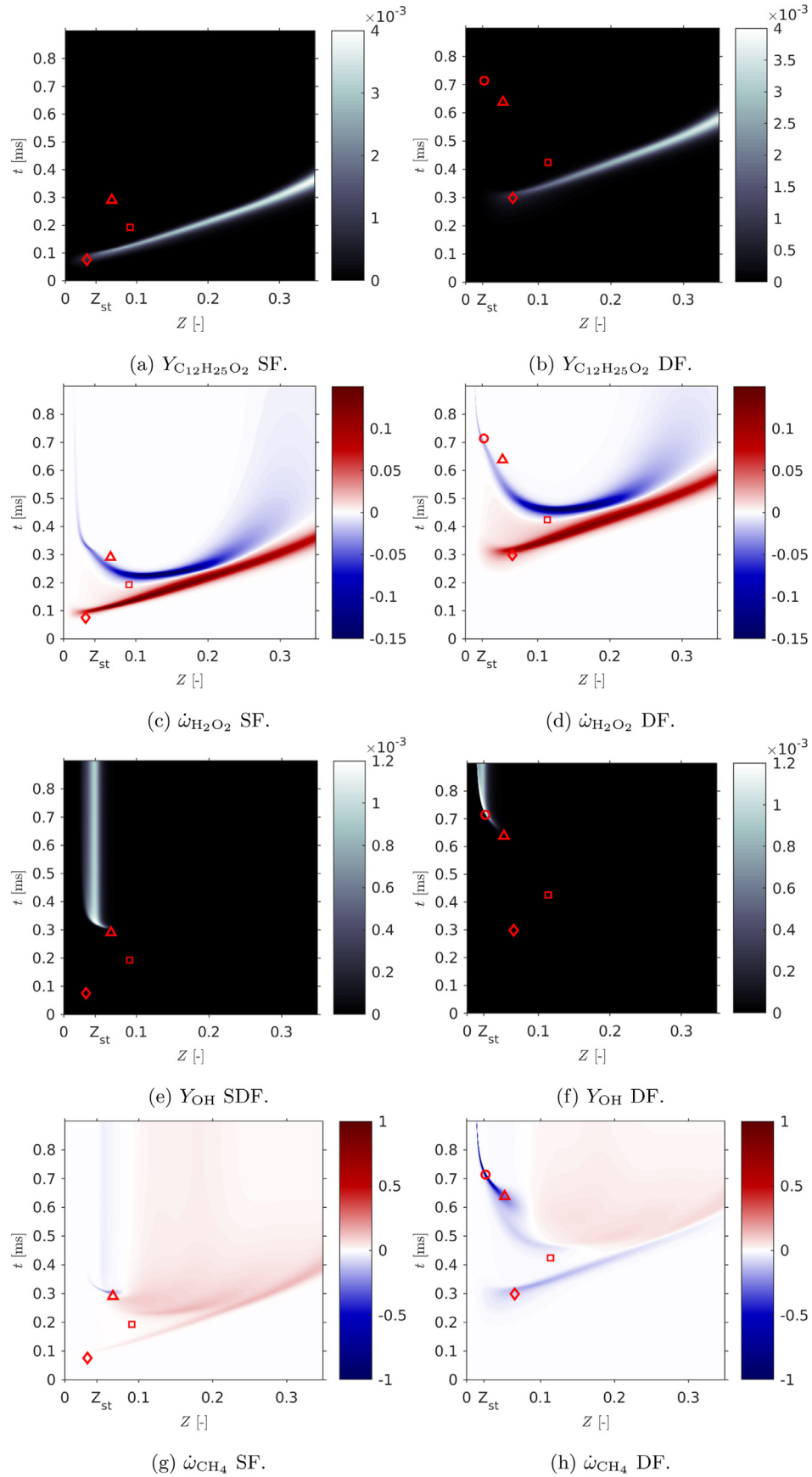
(a) $Y_{\mathrm{C_{12}H_{25}O_2}}$ SF.

(b) $Y_{\mathrm{C_{12}H_{25}O_2}}$ DF.

(c) $\dot{\omega}_{\mathrm{H_2O_2}}$ SF.

(d) $\dot{\omega}_{\mathrm{H_2O_2}}$ DF.

(e) Y_{OH} SDF.

(f) Y_{OH} DF.

(g) $\dot{\omega}_{\mathrm{CH_4}}$ SF.

(h) $\dot{\omega}_{\mathrm{CH_4}}$ DF.

Fig. C.1. Relevant species mass fractions (Y_i [-]) and net reaction rates ($\dot{\omega}_{Y_i}$ [$\mathrm{mole\,cm^3\,s^{-1}}$]) obtained from laminar flamelets in Zt-plane for SF and DF cases with the Yao mechanism. Point-pairs $Z\tau$ mark the first time instance when: $\widetilde{Y}_{\mathrm{RO_2}} > 20\%\max(\widetilde{Y}_{\mathrm{RO_2}})$ ◇, H_2O_2 consumption rate reaches 1% of its maximum □ and OH mass fraction △ and CH_4 consumption rate ◯ exceed 2% and 90% of their maximum, respectively.

References

[1] H.M. Cho, B.Q. He, Spark ignition natural gas engines – a review, Energy Convers. Manag. 48 (2) (2007) 608–618, doi:10.1016/j.enconman.2006.05.023.

[2] B.B. Sahoo, N. Sahoo, U.K. Saha, Effect of engine parameters and type of gaseous fuel on the performance of dual-fuel gas diesel engines – A critical review, Renew. Sustain. Energy Rev. 13 (6–7) (2009) 1151–1184, doi:10.1016/j.rser.2008.08.003.

[3] T. Korakianitis, A.M. Namasivayam, R.J. Crookes, Natural-gas fueled spark-ignition (SI) and compression-ignition (CI) engine performance and emissions, Progr. Energy Combust. Sci. 37 (1) (2011) 89–112, doi:10.1016/j.pecs.2010.04.002.

[4] G. Abd Alla, H. Soliman, O. Badr, M. Abd Rabbo, Effect of pilot fuel quantity on the performance of a dual fuel engine, Energy Convers. Manag. 41 (6) (2000) 559–572, doi:10.1016/S0196-8904(99)00124-7.

[5] L. Wei, P. Geng, A review on natural gas/diesel dual fuel combustion, emissions and performance, Fuel Process. Technol. 142 (2016) 264–278, doi:10.1016/j.fuproc.2015.09.018.

[6] M.S. Lounici, K. Loubar, L. Tarabet, M. Balistrou, D.C. Niculescu, M. Tazerout, Towards improvement of natural gas-diesel dual fuel mode: an experimental investigation on performance and exhaust emissions, Energy 64 (2014) 200–211, doi:10.1016/j.energy.2013.10.091.

[7] S. Imran, D.R. Emberson, A. Diez, D.S. Wen, R.J. Crookes, T. Korakianitis, Natural gas fueled compression ignition engine performance and emissions maps with diesel and RME pilot fuels, Appl. Thermal Eng. 67 (1–2) (2014) 354–365, doi:10.1016/j.apenergy.2014.02.067.

[8] J. Liu, F. Yang, H. Wang, M. Ouyang, S. Hao, Effects of pilot fuel quantity on the emissions characteristics of a CNG/diesel dual fuel engine with optimized pilot injection timing, Appl. Energy 110 (2013) 201–206, doi:10.1016/J.APENERGY.2013.03.024.

[9] O. Badr, G. Karim, B. Liu, An examination of the flame spread limits in a dual fuel engine, Appl. Thermal Eng. 19 (10) (1999) 1071–1080, doi:10.1016/S1359-4311(98)00108-2.

[10] M. Mbarawa, B.E. Milton, R.T. Casey, Experiments and modelling of natural gas combustion ignited by a pilot diesel fuel spray, Int. J. Thermal Sci. 40 (10) (2001) 927–936, doi:10.1016/S1290-0729(01)01279-0.

[11] G.H. Abd Alla, H.A. Soliman, O.A. Badr, M.F. Abd Rabbo, Effect of injection timing on the performance of a dual fuel engine, Energy Convers. Manag. 43 (2) (2002) 269–277, doi:10.1016/S0196-8904(00)00168-0.

[12] C.S. Lee, K.H. Lee, D.S. Kim, Experimental and numerical study on the combustion characteristics of partially premixed charge compression ignition engine with dual fuel, Fuel 82 (5) (2003) 553–560, doi:10.1016/S0016-2361(02)00319-8.

[13] G.A. Karim, Combustion in gas fueled compression: ignition engines of the dual fuel type, J. Eng. Gas Turb. Power 125 (3) (2003) 827, doi:10.1115/1.1581894.

[14] R.G. Papagiannakis, D.T. Hountalas, Combustion and exhaust emission characteristics of a dual fuel compression ignition engine operated with pilot diesel fuel and natural gas, Energy Convers. Manag. 45 (18–19) (2004) 2971–2987, doi:10.1016/j.enconman.2004.01.013.

[15] E. Tomita, Y. Harada, N. Kawahara, A. Sakane, Effect of EGR on combustion and exhaust emissions in supercharged dual-fuel natural gas engine ignited with diesel fuel, 2009, doi:10.4271/2009-01-1832. Technical paper 2009-01-1832.

[16] R.M. Hanson, S.L. Kokjohn, D.A. Splitter, R.D. Reitz, An experimental investigation of fuel reactivity controlled PCCI combustion in a heavy-duty engine, SAE Int. J. Eng. 3 (1) (2010) 700–716, doi:10.4271/2010-01-0864.

[17] U. Azimov, E. Tomita, N. Kawahara, Ignition, combustion and exhaust emission characteristics of micro-pilot ignited dual-fuel engine operated under premier combustion mode, SAETechnical Paper 2011-01-17(2011). doi:10.4271/2011-01-1764.

[18] D. Lata, A. Misra, Analysis of ignition delay period of a dual fuel diesel engine with hydrogen and LPG as secondary fuels, Int. J. Hydrog. Energy 36 (5) (2011) 3746–3756, doi:10.1016/J.IJHYDENE.2010.12.075.

[19] K. Ryu, Effects of pilot injection timing on the combustion and emissions characteristics in a diesel engine using biodieselCNG dual fuel, Appl. Energy 111 (2013) 721–730, doi:10.1016/J.APENERGY.2013.05.046.

[20] C. Aksu, N. Kawahara, K. Tsuboi, M. Kondo, E. Tomita, Extension of PREMIER combustion operation range using split micro pilot fuel injection in a dual fuel natural gas compression ignition engine: A performance-based and visual investigation, Fuel 185 (2016) 243–253, doi:10.1016/j.fuel.2016.07.120.

[21] R. Pettinen, O. Kaario, M. Larmi, Dual-fuel combustion characterization on lean conditions and high loads, SAETechnical Paper 2017-01-07(2017). doi:10.4271/2017-01-0759.

[22] Z. Ahmad, J. Aryal, O. Ranta, O. Kaario, V. Vuorinen, M. Larmi, An optical characterization of dual-fuel combustion in a heavy-duty diesel engine, SAETechnical Paper 2018-01-02(2018). doi:10.4271/2018-01-0252.

[23] X. Lü, Y. Hou, L. Zu, Z. Huang, Experimental study on the auto-ignition and combustion characteristics in the homogeneous charge compression ignition (HCCI) combustion operation with ethanol/n-heptane blend fuels by port injection, Fuel 85 (17–18) (2006) 2622–2631, doi:10.1016/J.FUEL.2006.05.003.

[24] S.L. Kokjohn, R.M. Hanson, D.A. Splitter, R.D. Reitz, Fuel reactivity controlled compression ignition (RCCI): a pathway to controlled high-efficiency clean combustion, Int. J. Eng. Res. 12 (3) (2011) 209–226, doi:10.1177/1468087411401548.

[25] D.E. Nieman, A.B. Dempsey, R.D. Reitz, Heavy-duty RCCI operation using natural gas and diesel, SAE Int. J. Eng. 5 (2) (2012) 270–285, doi:10.4271/2012-01-0379.

[26] Y. Li, M. Jia, Y. Chang, Y. Liu, M. Xie, T. Wang, L. Zhou, Parametric study and optimization of a RCCI (reactivity controlled compression ignition) engine fueled with methanol and diesel, Energy 65 (2014) 319–332, doi:10.1016/j.energy.2013.11.059.

[27] H. Saito, T. Sakurai, T. Sakonji, T. Hirashima, K. Kanno, Study on lean burn gas engine using pilot oil as the ignition source, SAETechnical Paper 2001-01-01 (2001). doi:10.4271/2001-01-0143.

[28] S. Schlatter, B. Schneider, Y. Wright, K. Boulouchos, Experimental study of ignition and combustion characteristics of a diesel pilot spray in a lean premixed methane/air charge using a rapid compression expansion machine, SAETechnical paper 2012-01-08 (2012). doi:10.4271/2012-01-0825.

[29] M. Rong, X. He, H. Liu, Y. Shang, W. Zeng, X. Li, F. Liu, An optical investigation on the combustion characteristics of gasoline-diesel dual-fuel applications, SAETechnical Paper 2014-01-13 (2014), doi:10.4271/2014-01-1310.

[30] N. Dronniou, J. Kashdan, B. Lecointe, K. Sauve, D. Soleri, Optical investigation of dual-fuel CNG/diesel combustion strategies to reduce CO2 emissions, SAE Int. J. Eng. 7 (2) (2014) 873–887, doi:10.4271/2014-01-1313.

[31] X. Ma, Y. Qi, Z. Wang, H. Xu, J. Wang, An experimental study of EGR-controlled stoichiometric dual-fuel compression ignition (SDCI) combustion, SAETechnical Paper 2014-01-13 (2015). doi:10.4271/2014-01-1307.

[32] S. Schlatter, B. Schneider, Y. Wright, K. Boulouchos, N-heptane micro pilot assisted methane combustion in a rapid compression expansion machine, Fuel 179 (2016) 339–352, doi:10.1016/j.fuel.2016.03.006.

[33] A. Srna, G. Bruneaux, B. von Rotz, R. Bombach, K. Herrmann, K. Boulouchos, Optical investigation of sooting propensity of n- dodecane pilot/lean-premixed methane dual- fuel combustion in a rapid compression- expansion machine, SAETechnical Paper 2018-01-02(2018). 10.4271/2018-01-0258.

[34] A. Srna, M. Bolla, Y.M. Wright, K. Herrmann, R. Bombach, S.S. Pandurangi, K. Boulouchos, G. Bruneaux, Effect of methane on pilot-fuel auto-ignition in dual-fuel engines, Proc. Combust. Inst. (2018), doi:10.1016/J.PROCI.2018.06.177.

[35] S. Schlatter, Experimental and numerical characterization of enhanced ignition systems for large bore gas engines, ETH-Zürich, 2015 Ph.D. thesis.

[36] M. Ghaderi Masouleh, A. Wehrfritz, O. Kaario, H. Kahila, V. Vuorinen, Comparative study on chemical kinetic schemes for dual-fuel combustion of n-dodecane/methane blends, Fuel 191 (2017) 62–76, doi:10.1016/j.fuel.2016.10.114.

[37] G.H. Abd Alla, H.A. Soliman, O.A. Badr, M.F. Abd Rabbo, Combustion quasi-two zone predictive model for dual fuel engines, Energy Convers. Manag. 42 (12) (2001) 1477–1498, doi:10.1016/S0196-8904(00)00143-6.

[38] A. Maghbouli, R.K. Saray, S. Shafee, J. Ghafouri, Numerical study of combustion and emission characteristics of dual-fuel engines using 3D-CFD models coupled with chemical kinetics, Fuel 106 (2013) 98–105, doi:10.1016/J.FUEL.2012.10.055.

[39] J. Li, W.M. Yang, T.N. Goh, H. An, A. Maghbouli, Study on RCCI (reactivity controlled compression ignition) engine by means of statistical experimental design, Energy 78 (2014) 777–787, doi:10.1016/j.energy.2014.10.071.

[40] A. Bhagatwala, R. Sankaran, S. Kokjohn, J.H. Chen, Numerical investigation of spontaneous flame propagation under RCCI conditions, Combust. Flame 162 (9) (2015) 3412–3426, doi:10.1016/j.combustflame.2015.06.005.

[41] V. Fraioli, C. Beatrice, G. Di Blasio, G. Belgiorno, M. Migliaccio, Multidimensional simulations of combustion in methane-diesel dual-fuel light-duty engines, SAETechnical Paper 2017-01-05(2017). 10.4271/2017-01-0568.

[42] E. Demosthenous, G. Borghesi, E. Mastorakos, R.S. Cant, Direct numerical simulations of premixed methane flame initiation by pilot n-heptane spray autoignition, Combust. Flame 163 (2016) 122–137, doi:10.1016/j.combustflame.2015.09.013.

[43] Z. Wang, J. Abraham, Fundamental physics of flame development in an autoigniting dual fuel mixture, Proc. Combust. Inst. 35 (1) (2015) 1041–1048, doi:10.1016/j.proci.2014.06.079.

[44] G. Borghesi, E. Mastorakos, R.S. Cant, Complex chemistry DNS of n-heptane spray autoignition at high pressure and intermediate temperature conditions, Combust. Flame 160 (7) (2013) 1254–1275, doi:10.1016/j.combustflame.2013.02.009.

[45] U. Burke, K.P. Somers, P. O'Toole, C.M. Zinner, N. Marquet, G. Bourque, E.L. Petersen, W.K. Metcalfe, Z. Serinyel, H.J. Curran, An ignition delay and kinetic modeling study of methane, dimethyl ether, and their mixtures at high pressures, Combust. Flame 162 (2) (2015) 315–330, doi:10.1016/j.combustflame.2014.08.014.

[46] A. Rahimi, E. Fatehifar, R.K. Saray, Development of an optimized chemical kinetic mechanism for homogeneous charge compression ignition combustion of a fuel blend of n-heptane and natural gas using a genetic algorithm, Proc. Inst. Mech. Eng. Part D J. Autom. Eng. 224 (9) (2010) 1141–1159, doi:10.1243/09544070JAUTO1343.

[47] Engine combustion network, Combustion research facility, Sandia national laboratories, Livermore, CA, (2018) See https://ecn.sandia.gov. Accessed May 2018.

[48] L.M. Pickett, C.L. Genzale, G. Bruneaux, L. Malbec, L. Hermant, C. Christiansen, J. Schramm, Comparison of diesel spray combustion in different high-temperature, high-pressure facilities, SAE Int. J. Eng. 3 (2) (2010) 2010–01–2106, doi:10.4271/2010-01-2106.

[49] R. Payri, J.M. García-Oliver, M. Bardi, J. Manin, Fuel temperature influence on diesel sprays in inert and reacting conditions, Appl. Thermal Eng. 35 (1) (2012) 185–195, doi:10.1016/j.applthermaleng.2011.10.027.

[50] M. Bardi, T. Bazyn, G. Bruneaux, J. Johnson, S. Lee, L.M. Malbec, M. Meijer, J. Naber, R. Payri, L.M. Pickett, B. Somers, Engine combustion network (ECN): characterization and comparison of boundary conditions for different combustion vessels, At. Sprays 22 (9) (2012) 777–806, doi:10.1615/AtomizSpr.2012006083.

[51] M. Bardi, R. Payri, L.M. Malbec, G. Bruneaux, L.M. Pickett, J. Manin, T. Bazyn, C. Genzale, Engine combustion network: comparison of spray development, vaporization, and combustion in different combustion vessels, At. Sprays 22 (10) (2012) 807–842, doi:10.1615/AtomizSpr.2013005837.

[52] J. Benajes, R. Payri, M. Bardi, P. Martí-Aldaraví, Experimental characterization of diesel ignition and lift-off length using a single-hole ECN injector, Appl. Thermal Eng. 58 (1–2) (2013) 554–563, doi:10.1016/j.applthermaleng.2013.04.044.

[53] N. Maes, M. Meijer, N. Dam, B. Somers, H. Baya Toda, G. Bruneaux, S.A. Skeen, L.M. Pickett, J. Manin, Characterization of Spray A flame structure for parametric variations in ECN constant-volume vessels using chemiluminescence and laser-induced fluorescence, Combust. Flame 174 (2016) 138–151, doi:10.1016/j.combustflame.2016.09.005.

[54] S.A. Skeen, J. Manin, L.M. Pickett, Simultaneous formaldehyde PLIF and high-speed schlieren imaging for ignition visualization in high-pressure spray flames, Proc. Combust. Inst. 35 (3) (2015) 3167–3174, doi:10.1016/j.proci.2014.06.040.

[55] Q. Xue, S. Som, P.K. Senecal, E. Pomraning, Large eddy simulation of fuel spray under non-reacting ic engine conditions, At. Sprays 23 (10) (2013) 1–30, doi:10.1615/AtomizSpr.2013008320.

[56] S. Bhattacharjee, D.C. Haworth, Simulations of transient n-heptane and n-dodecane spray flames under engine-relevant conditions using a transported PDF method, Combust. Flame 160 (10) (2013) 2083–2102, doi:10.1016/j.combustflame.2013.05.003.

[57] A. Wehrfritz, V. Vuorinen, O. Kaario, M. Larmi, Large eddy simulation of high-velocity fuel sprays: studying mesh resolution and breakup model effects for spray A, At. Sprays 23 (5) (2013) 419–442, doi:10.1615/AtomizSpr.2013007342.

[58] G. D'Errico, T. Lucchini, F. Contino, M. Jangi, X. Bai, Comparison of well-mixed and multiple representative interactive flamelet approaches for diesel spray combustion modelling, Combust. Theory Modell. 18 (1) (2014) 65–88, doi:10.1080/13647830.2013.860224.

[59] P. Kundu, Y. Pei, M. Wang, R. Mandhapati, S. Som, Evaluation of turbulence-chemistry interaction under diesel engine conditions with multi-flamelet RIF model, At. Sprays 24 (9) (2014) 779–800, doi:10.1615/AtomizSpr.2014010506.

[60] C. Gong, M. Jangi, X. Bai, Large eddy simulation of n-dodecane spray combustion in a high pressure combustion vessel, Appl. Energy 136 (2014) 373–381, doi:10.1016/j.apenergy.2014.09.030.

[61] C. Gong, M. Jangi, T. Lucchini, G. D'Errico, X.S. Bai, Large eddy simulation of air entrainment and mixing in reacting and non-reacting diesel sprays, Flow Turbul. Combust. 93 (3) (2014) 385–404, doi:10.1007/s10494-014-9566-0.

[62] S. Banerjee, C.J. Rutland, Study on spray induced turbulence using large eddy simulation, At. Sprays 25 (4) (2015) 285–316, doi:10.1615/AtomizSpr.2015006910.

[63] Y. Pei, E.R. Hawkes, S. Kook, G.M. Goldin, T. Lu, Modelling n-dodecane spray and combustion with the transported probability density function method, Combust. Flame 162 (5) (2015) 2006–2019, doi:10.1016/j.combustflame.2014.12.019.

[64] Y. Pei, S. Som, E. Pomraning, P.K. Senecal, S.A. Skeen, J. Manin, L.M. Pickett, Large eddy simulation of a reacting spray flame with multiple realizations under compression ignition engine conditions, Combust. Flame 162 (12) (2015) 4442–4455, doi:10.1016/j.combustflame.2015.08.010.

[65] R. Payri, J.P. Viera, Y. Pei, S. Som, Experimental and numerical study of lift-off length and ignition delay of a two-component diesel surrogate, Fuel 158 (2015) 957–967, doi:10.1016/j.fuel.2014.11.072.

[66] C.K. Blomberg, L. Zeugin, S.S. Pandurangi, M. Bolla, K. Boulouchos, Y.M. Wright, Modeling split injections of ECN spray ag using a conditional moment closure combustion model with RANS and LES, SAE Int. J. Eng. 9 (4) (2016) 2107–2119, doi:10.4271/2016-01-2237.

[67] L. Hakim, G. Lacaze, J. Oefelein, Large eddy simulation of autoignition transients in a model diesel injector configuration, SAE Int. J. Fuels Lubr. 9 (1) (2016) 165–176, doi:10.4271/2016-01-0872.

[68] A. Wehrfritz, O. Kaario, V. Vuorinen, B. Somers, Large eddy simulation of n-dodecane spray flames using flamelet generated manifolds, Combust. Flame 167 (2016) 113–131, doi:10.1016/j.combustflame.2016.02.019.

[69] R.N. Dahms, G.A. Paczko, S.A. Skeen, L.M. Pickett, Understanding the ignition mechanism of high-pressure spray flames, Proc. Combust. Inst. 36 (2) (2016) 2615–2623, doi:10.1016/j.proci.2016.08.023.

[70] H. Kahila, A. Wehrfritz, O. Kaario, M. Ghaderi Masouleh, N. Maes, B. Somers, V. Vuorinen, Large-eddy simulation on the influence of injection pressure in reacting Spray A, Combust. Flame 191 (2018) 142–159, doi:10.1016/j.COMBUSTFLAME.2018.01.004.

[71] H. Jasak, H.G. Weller, A.D. Gosman, High resolution NVD differencing scheme for arbitrarily unstructured meshes, Int. J. Numer. Methods Fluids 31 (2) (1999) 431–449, doi:10.1002/(SICI)1097-0363(19990930)31:2<431::AID-FLD884>3.0.CO;2-T.

[72] R. Issa, B. Ahmadi-Befrui, K. Beshay, A. Gosman, Solution of the implicitly discretised reacting flow equations by operator-splitting, J. Comput. Phys. 93 (2) (1991) 388–410, doi:10.1016/0021-9991(91)90191-M.

[73] R.D. Reitz, Modeling atomization processes in high-pressure vaporizing sprays, At. Spray Technol. 3 (1987) 309–337.

[74] R.D. Reitz, J.C. Beale, Modeling spray atomization With the Kelvin-Helmholtz/Rayleigh-Taylor hybrid model, At. Sprays 9 (6) (1999) 623–650, doi:10.1615/AtomizSpr.v9.i6.40.

[75] N. Frossling, Evaporation, heat transfer, and velocity distribution in two-dimensional and rotationally symmetrical laminar boundary-layer flow, Technical Report ADB1891, N.A.C.A., 1956.

[76] W.E. Ranz, W.R. Marshall, Evaporation from drops, part I, Chem. Eng. Progr. 48 (3) (1952) 141–146.

[77] W. Ranz, W. Marshall, Evaporation from drops, part II, Chem. Eng. Progr. 48 (3) (1952) 173–180.

[78] The open source computational fluid dynamics (CFD) toolbox. (2018) OpenFOAM Foundation Available at: http://www.openfoam.org. Accessed May 2018.

[79] F.F. Grinstein, L.G. Margolin, W. Rider, Implicit large eddy simulation: computing turbulent fluid dynamics, Cambridge University Press, 2007.

[80] F.F. Grinstein, C. Fureby, On flux-limiting-based implicit large eddy simulation, J. Fluids Eng. 129 (12) (2007) 1483, doi:10.1115/1.2801684.

[81] A. Aspden, N. Nikiforakis, S. Dalziel, J. Bell, Analysis of implicit LES methods, Commun. Appl. Math. Comput. Sci. 3 (1) (2008) 103–126, doi:10.2140/camcos.2008.3.103.

[82] C. Fureby, F.F. Grinstein, Large eddy simulation of high-Reynolds-number free and wall-bounded flows, J. Comput. Phys. 181 (1) (2002) 68–97, doi:10.1006/jcph.2002.7119.

[83] C. Fureby, F. Grinstein, Monotonically integrated large eddy simulation of free shear flows, AIAA J. 37 (5) (1999) 544–556, doi:10.2514/2.772.

[84] V. Vuorinen, J. Yu, S. Tirunagari, O. Kaario, M. Larmi, C. Duwig, B.J. Boersma, Large-eddy simulation of highly underexpanded transient gas jets, Phys. Fluids 25 (1) (2013) 016101, doi:10.1063/1.4772192.

[85] V. Vuorinen, A. Wehrfritz, C. Duwig, B.J. Boersma, Large-eddy simulation on the effect of injection pressure and density on fuel jet mixing in gas engines, Fuel 130 (2014) 241–250, doi:10.1016/j.fuel.2014.04.045.

[86] M. Berglund, C. Fureby, LES of supersonic combustion in a scramjet engine model, Proc. Combust. Inst. 31 II (2) (2007) 2497–2504, doi:10.1016/j.proci.2006.07.074.

[87] M.S. Day, J.B. Bell, Numerical simulation of laminar reacting flows with complex chemistry, Combust. Theory Modell. 4 (4) (2000) 535–556, doi:10.1088/1364-7830/4/4/309.

[88] Z. Lu, H. Zhou, S. Li, Z. Ren, T. Lu, C.K. Law, Analysis of operator splitting errors for near-limit flame simulations, J. Comput. Phys. 335 (2017) 578–591, doi:10.1016/j.jcp.2017.01.044.

[89] B. Sportisse, An analysis of operator splitting techniques in the stiff case, J. Comput. Phys. 161 (1) (2000) 140–168, doi:10.1006/jcph.2000.6495.

[90] K.E. Niemeyer, N.J. Curtis, C. Sung, pyJac: analytical Jacobian generator for chemical kinetics, Comput. Phys. Commun. 215 (2017) 188–203, doi:10.1016/J.CPC.2017.02.004.

[91] E. Hairer, G. Wanner, Solving ordinary differential equations. II, Springer-Verlag, 1996, doi:10.1007/978-3-642-05221-7.

[92] A. Imren, D.C. Haworth, On the merits of extrapolation-based stiff ODE solvers for combustion CFD, Combust. Flame 174 (2016) 1–15, doi:10.1016/j.combustflame.2016.09.018.

[93] G. Strang, On the construction and comparison of difference schemes, SIAM J. Numer. Anal. 5 (3) (1968) 506–517, doi:10.1137/0705041.

[94] F. Qin, A. Shah, Z. Huang, L. Peng, P. Tunestal, X. Bai, Detailed numerical simulation of transient mixing and combustion of premixed methane/air mixtures in a pre-chamber/main-chamber system relevant to internal combustion engines, Combust. Flame 188 (2018) 357–366, doi:10.1016/j.combustflame.2017.10.006.

[95] J. J. Behzadi, M. Talei, M. Bolla, E.R. Hawkes, T. Lucchini, S. Kook, A conditional moment closure study of chemical reaction source terms in SCCI combustion, Flow Turbul. Combust. 100 (2018) 93–118, doi:10.1007/s10494-017-9825-y.

[96] C. Duwig, K. Nogenmyr, C. Chan, M.J. Dunn, Large eddy simulations of a piloted lean premix jet flame using finite-rate chemistry, Combust. Theory Modell. 15 (4) (2011) 537–568, doi:10.1080/13647830.2010.548531.

[97] E. Fedina, C. Fureby, G. Bulat, W. Meier, Assessment of finite rate chemistry large eddy simulation combustion models, Flow Turbul. Combust. 99 (99) (2017), doi:10.1007/s10494-017-9823-0.

[98] E. Anderson, Z. Bai, C. Bischof, S. Blackford, J. Demmel, J. Dongarra, J. Du Croz, A. Greenbaum, S. Hammarling, A. McKenney, D. Sorensen, LAPACK users' guide, third ed., Society for Industrial and Applied Mathematics, 1996.

[99] A. Varna, A. Wehrfritz, E. R. Hawkes, M. J. Cleary, T. Lucchini, G. D'Errico, S. Kook, Q. N. Chan, Application of a multiple mapping conditioning mixing model to ECN Spray A, Proc. Combust. Inst. (2018), doi:10.1016/J.PROCI.2018.06.007.

[100] C. Eberle, P. Gerlinger, K.P. Geigle, M. Aigner, Toward finite-rate chemistry large-eddy simulations of sooting swirl flames, Combust. Sci. Technol. (2018) 1–24, doi:10.1080/00102202.2018.1443444.

[101] J.R. Edwards, J.A. Boles, R.A. Baurle, Large-eddy/Reynolds-averaged Navier–Stokes simulation of a supersonic reacting wall jet, Combust. Flame 159 (3) (2012) 1127–1138, doi:10.1016/J.COMBUSTFLAME.2011.10.009.

[102] E. Hodzic, E. Alenius, C. Duwig, R.S. Szasz, L. Fuchs, A large eddy simulation study of bluff body flame dynamics approaching blow-off, Combust. Sci. Technol. 189 (7) (2017) 1107–1137, doi:10.1080/00102202.2016.1275592.

[103] J.A. Fulton, J.R. Edwards, A. Cutler, J. McDaniel, C. Goyne, Turbulence/chemistry interactions in a ramp-stabilized supersonic hydrogen-air diffusion flame, Combust. Flame 174 (2016) 152–165, doi:10.1016/J.COMBUSTFLAME.2016.09.017.

[104] C. Fureby, Comparison of flamelet and finite rate chemistry LES for premixed turbulent combustion, 45th AIAA Aerospace Sciences Meeting and Exhibit, 24, American Institute of Aeronautics and Astronautics, Reston, Virigina (2007), pp. 1–16, doi:10.2514/6.2007-1413.

[105] F. Bottone, A. Kronenburg, D. Gosman, A. Marquis, The numerical simulation of diesel spray combustion with LES-CMC, Flow Turbul. Combust. 89 (4) (2012) 651–673, doi:10.1007/s10494-012-9415-y.

[106] A. Irannejad, A. Banaeizadeh, F. Jaberi, Large eddy simulation of turbulent spray combustion, Combust. Flame 162 (2) (2015) 431–450, doi:10.1016/j.combustflame.2014.07.029.

[107] S. Gallot-Lavallée, W.P. Jones, Large eddy simulation of spray auto-ignition under EGR conditions, Flow Turbul. Combust. 96 (2) (2016) 513–534, doi:10.1007/s10494-015-9684-3.

[108] CMT Virtual Injection Rate Generator. (2018) Available at: https://www.cmt.upv.es/ecn03.aspx. Accessed: May 2018.

[109] R.W. Bilger, S.H. Stårner, R.J. Kee, On reduced mechanisms for methane-air combustion in nonpremixed flames, Combust. Flame 80 (2) (1990) 135–149, doi:10.1016/0010-2180(90)90122-8.

[110] J.C. Sutherland, P.J. Smith, J.H. Chen, Quantification of differential diffusion in nonpremixed systems, Combust. Theory Modell. 9 (2) (2005) 365–383, doi:10.1080/17455030500150009.

[111] T. Yao, Y. Pei, B. Zhong, S. Som, T. Lu, K.H. Luo, A compact skeletal mechanism for n-dodecane with optimized semi-global low-temperature chemistry for diesel engine simulations, Fuel 191 (2017) 339–349, doi:10.1016/j.fuel.2016.11.083.

[112] A. Frassoldati, G. D'Errico, T. Lucchini, A. Stagni, A. Cuoci, T. Faravelli, A. Onorati, E. Ranzi, Reduced kinetic mechanisms of diesel fuel surrogate for engine CFD simulations, Combust. Flame 162 (10) (2015) 3991–4007, doi:10.1016/j.combustflame.2015.07.039.

[113] J.M. Desantes, J.J. López, J.M. García-Oliver, D. López-Pintor, Experimental validation and analysis of seven different chemical kinetic mechanisms for n-dodecane using a Rapid Compression-Expansion Machine, Combust. Flame 182 (2017) 76–89, doi:10.1016/j.combustflame.2017.04.004.

[114] E.R. Hawkes, Ignition and flame structure, 5th workshop of the Engine Combustion Network, Detroit, USA, 2017. Available at www.sandia.gov/ecn. Accessed Jan. 2018.

[115] D.M. Manias, E.A. Tingas, C.E. Frouzakis, K. Boulouchos, D.A. Goussis, The mechanism by which CH2O and H2O2 additives affect the autoignition of CH4/air mixtures, Combust. Flame 164 (2016) 111–125, doi:10.1016/j.combustflame.2015.11.008.

[116] E.L. Petersen, D.F. Davidson, R.K. Hanson, Kinetics modeling of shock-induced ignition in low-dilution CH4/O2 mixtures at high pressures and intermediate temperatures, Combust. Flame 117 (1–2) (1999) 272–290, doi:10.1016/S0010-2180(98)00111-4.

[117] W.K. Metcalfe, S.M. Burke, S.S. Ahmed, H.J. Curran, A hierarchical and comparative kinetic modeling study of C1-C2 hydrocarbon and oxygenated fuels, Int. J. Chem. Kinet. 45 (10) (2013) 638–675, doi:10.1002/kin.20802.

[118] G.P. Smith, David M. Golden, M. Frenklach, N.W. Moriarty, B. Eiteneer, M. Goldenberg, C.T. Bowman, R.K. Hanson, S. Song, J.W.C. Gardiner, V.V. Lissianski, Z. Qin, V.V. Lissianski, G.P. Smith, David M. Golden, M. Frenklach, N.W. Moriarty, B. Eiteneer, M. Goldenberg, C.T. Bowman, R.K. Hanson, S. Song, J.W.C. Gardiner Jr., Z. Qin, GRI-3.0 mechanism, (2018) Available at: http://www.combustion.berkeley.edu/gri-mech/version30/text30.html. Accessed May 2018.

[119] E. Mastorakos, Ignition of turbulent non-premixed flames, Progr. Energy Combust. Sci. 35 (1) (2009) 57–97, doi:10.1016/j.pecs.2008.07.002.

[120] Y. Pei, E.R. Hawkes, M. Bolla, S. Kook, G.M. Goldin, Y. Yang, S.B. Pope, S. Som, An analysis of the structure of an n-dodecane spray flame using TPDF modelling, Combust. Flame 168 (2016) 420–435, doi:10.1016/j.combustflame.2015.11.034.

[121] B. Akkurt, H.Y. Akargun, L.M.T. Somers, N.G. Deen, R. Novella, E.J. Pérez-Sánchez, An insight on the spray-a combustion characteristics by means of rans and les simulations using flamelet-based combustion models, SAETechnical Paper 2017-01-05(2017). 10.4271/2017-01-0577.

[122] C.K. Westbrook, Chemical kinetics of hydrocarbon ignition in practical combustion systems, Proc. Combust. Inst. 28 (2) (2000) 1563–1577, doi:10.1016/S0082-0784(00)80554-8.

[123] A. Krisman, E.R. Hawkes, M. Talei, A. Bhagatwala, J.H. Chen, Characterisation of two-stage ignition in diesel engine-relevant thermochemical conditions using direct numerical simulation, Combust. Flame 172 (2016) 326–341, doi:10.1016/j.combustflame.2016.06.010.

[124] G. Dixon-Lewis, T. David, P.H. Gaskell, S. Fukutani, H. Jinno, J.A. Miller, R.J. Kee, M.D. Smooke, N. Peters, E. Effelsberg, J. Warnatz, F. Behrendt, Calculation of the structure and extinction limit of a methane-air counterflow diffusion flame in the forward stagnation region of a porous cylinder, Symp. (Int.) Combust. 20 (1) (1985) 1893–1904, doi:10.1016/S0082-0784(85)80688-3.

[125] L. De Goey, J. Ten Thije Boonkkamp, A mass-based definition of flame stretch for flames with finite thickness, Combust. Sci. Technol. 122 (1–6) (1997) 399–405, doi:10.1080/00102209708935618.

[126] Chem1D – a one-dimensional laminar flame code, Eindhoven University of Technology. (2018) Available at www.combustion.tue.nl. Accessed May 2018.

[127] K. Narayanaswamy, P. Pepiot, H. Pitsch, A chemical mechanism for low to high temperature oxidation of n-dodecane as a component of transportation fuel surrogates, Combust. Flame 161 (4) (2014) 866–884, doi:10.1016/j.combustflame.2013.10.012.

[128] S.S. Vasu, D.F. Davidson, Z. Hong, V. Vasudevan, R.K. Hanson, n-dodecane oxidation at high-pressures: measurements of ignition delay times and OH concentration time-histories, Proc. Combust. Inst. 32 I (1) (2009) 173–180, doi:10.1016/j.proci.2008.05.006.

[129] H.P.S. Shen, J. Steinberg, J. Vanderover, M.A. Oehlschlaeger, A Shock tube study of the ignition of n-heptane, n-decane, n-dodecane, and n-tetradecane at elevated pressures, Energy Fuels 23 (5) (2009) 2482–2489, doi:10.1021/ef8011036.

[130] L.M. Pickett, J. Manin, C.L. Genzale, D.L. Siebers, M.P.B. Musculus, C.A. Idicheria, Relationship between diesel fuel spray vapor penetration/dispersion and local fuel mixture fraction, SAE Int. J. Eng. 4 (1) (2011) 764–799, doi:10.4271/2011-01-0686.